PHYSICAL REVIEW B **109**, 224506 (2024)

Superfluidity of indirect momentum space dark dipolar excitons in a double layer with anisotropic tilted semi-Dirac bands

A. Nafis Arafat,[1,2,*] Oleg L. Berman,[1,3] and Godfrey Gumbs[1,2,4]
[1]*The Graduate School and University Center, The City University of New York, 365 Fifth Avenue, New York, New York 10016, USA*
[2]*Department of Physics and Astronomy, Hunter College of The City University of New York, 695 Park Avenue, New York, New York 10065, USA*
[3]*Physics Department, New York City College of Technology, The City University of New York, 300 Jay Street, Brooklyn, New York 11201, USA*
[4]*Donostia International Physics Center (DIPC), P de Manuel Lardizabal, 4, 20018 San Sebastian, Basque Country, Spain*

(Received 9 February 2024; revised 24 April 2024; accepted 22 May 2024; published 12 June 2024)

We have theoretically investigated the spin- and valley-dependent superfluid properties of indirect momentum space dark dipolar excitons in double layers with massive anisotropic tilted semi-Dirac energy bands in the presence of circularly polarized irradiation. An external vertical electric field is also applied to the structure and is responsible for tilting and gap opening of the energy bands. In our numerical calculations, we employed the parameters appropriate for a double layer of 1T′ -MoS$_2$. Closed form analytical expressions are presented for the energy spectrum for excitons, their associated wave functions and binding energies. Additionally, we examine the effects which varying the intensity and frequency of circularly polarized irradiation has for 1T′-MoS$_2$ on the effective mass of the excitons since it has been demonstrated that the application of an external high-frequency dressing field could tailor the crucial electronic properties including the exciton binding energy as well as the critical temperature for superfluidity. We also calculated the sound velocity in the anisotropic weakly interacting Bose gas of two-component indirect momentum space dark excitons for a double layer of 1T′-MoS$_2$. We show that the critical velocity of superfluidity, the spectrum of collective excitations, concentrations of the superfluid and normal component, and mean field critical temperature for superfluidity are anisotropic and formed by a two-component system. The critical temperature for superfluidity is increased when the exciton concentration and interlayer separation are increased. We propose the use of phonon-assisted photoluminescence to experimentally confirm directional superfluidity of indirect momentum space dark excitons in a double layer with massive anisotropic tilted semi-Dirac energy bands.

DOI: 10.1103/PhysRevB.109.224506

I. INTRODUCTION

Transition metal dichalcogenides (TMDCs) have been gaining much attention in recent times for their remarkable optoelectronic as well as transport properties. TMDCs have been found to have applications for a range of fundamental phenomena [1,2]. These materials can sustain the formation of polaritons at room temperature due to their relatively larger binding energy [3]. The condensation of paired objects due to repulsive interactions have been investigated in novel arenas such as two layers of Dirac electron gas [4]. Indirect momentum space dark excitons in a monolayer with massive anisotropic tilted semi-Dirac bands have been the subject of recent experimental studies [5–7]. So far, massive anisotropic tilted Dirac systems such as 1T′-MoS$_2$ are one of the more interesting 2D Dirac materials, due to their thermodynamic stability and their ease of synthesis in the semiconducting phase. Additionally, 1T′-MoS$_2$ has been predicted to display a strong quantum-spin Hall effect [8]. When a uniform perpendicular external electric field is applied, it exhibits valley-spin polarized Dirac bands [9] as well as a phase transition between a topological insulator and regular band insulator [10]. The anisotropy of the energy band structure is consequential due to its tilted and shifted valence and conduction Dirac bands [11]. The valley dependent physical properties of TMDCs make them an interesting candidate for valleytronics applications [12,13]. Additionally the properties of 2D TMDCs lends themselves well to energy storage [14], and photovoltaic applications [15].

Bose-Einstein condensation (BEC) occurs when bosons at low temperatures occupy the lowest energy quantum state. Due to the relatively large exciton binding energies in 2D semiconductors, such as 1T′-MoS$_2$, BEC and superfluidity of dipolar excitons in double layer 1T′-MoS$_2$ are possible. Since the de Broglie wavelength for a 2D system is inversely proportional to the square root of the mass of a particle, BEC is more likely to exist for bosons of larger mass at higher temperatures than for bosons with smaller mass. A Bose-Einstein condensate of weakly interacting particles was famously achieved experimentally in a dilute gas of alkali atoms, albeit at challengingly low temperatures in the nanokelvin regime [16]. Therefore BEC may exist at much higher temperatures in a Bose gas consisting of particles whose masses are smaller than those in a system of relatively heavy alkali atoms. There is also strong experimental evidence for exciton condensation in double layers of TMDCs [17]. Three-dimensional superfluidity has also been robustly predicted for a superlattice of alternating doped monolayers [18]. The BEC and superfluidity of dipolar bright excitons was predicted for double layers

---

[*] Corresponding author: aarafat@gradcenter.cuny.edu

in Ref. [19] and discussed for the double layers of TMDCs in Refs. [20–22]. The BEC and superfluidity of dipolar indirect momentum space excitons are intriguing due to the fact that we expect that such excitons will possess a higher lifetime than regular dipolar excitons. This is due to their recombination with photon emission is forbidden by selection rules [23]. In this paper, we develop an approach to study the superfluidity of a two-component dilute Bose gas of dipolar excitons in a double layer of massive anisotropic Dirac systems with tilted bands. While we perform our calculations for the selected case of a double layer of tilted 1T′-MoS$_2$, our approach can be applied to other massive anisotropic tilted Dirac systems without loss of generality. We investigate three different types of excitons. These are based on their spin and valley polarizations as well as the way in which they alter the effective masses and total masses of the excitons. Recent studies have shown that exploiting an imbalance of electron and hole effective masses can lead to the formation of exotic superfluid phases [24] including the Fulde-Ferrell-Larkin-Ovchinnikov (FFLO) phase as well as the Sarma phase [25,26]. We also study the effect which chosen parameters have on the binding energy of the three different types of excitons. Specifically, we analyze the way in which varying the relative value of the perpendicular electric field affects the binding energy. From this, we gain insight regarding the use of a number of dielectric layers (in our case hexagonal boron nitride, h-bN), for experimental exploration and their associated effects [27].

The rest of this paper is organized as follows. In Sec. II, the two-body problem for an electron and a hole, spatially separated in two parallel monolayers of 1T′-MoS$_2$, is formulated. The wave function and binding energy for a single dipolar exciton in the 1T′-MoS$_2$ double layer are calculated. In Sec. III, we investigate the conditions for the existence of collective excitations for spatially separated electrons and holes. In Sec. IV, we turn our attention to the case of two-component exciton superfluidity and we discuss the spectrum of collective excitations. Supplemental calculations to this section are presented in Ref. [28]. Section V is devoted to a discussesion of our results obtained for the exciton superfluidity. We propose a way to experimentally observe the indirect-momentum space dark excitons and related phenomena. Section VI contains our concluding remarks.

II. THE INTERACTING ELECTRON-HOLE PAIR

We begin by computing the wave functions and energy eigenvalues of the massive anisotropic tilted Dirac systems by examining the general Hamiltonian [30]. By examining the energy dispersion relation, and modifying it to the form of the model Hamiltonian for 1T′-MoS$_2$ with tilted Dirac bands, we are able to solve exactly for the analytical solution of the system. The model Hamiltonian within the effective mass approximation for a single electron-hole pair in a 1T′-MoS$_2$ double layer is given by [9]

$$\hat{H}_0 = -\frac{\hbar^2}{2m_x^e}\frac{\partial^2}{\partial x_1^2} - \frac{\hbar^2}{2m_y^e}\left[\frac{\partial}{\partial y_1} - p_e^{(0)}\right]^2 - \frac{\hbar^2}{2m_x^h}\frac{\partial^2}{\partial x_2^2} - \frac{\hbar^2}{2m_y^h}\left[\frac{\partial}{\partial y_2} - p_h^{(0)}\right]^2 + V(\sqrt{r^2 + D^2}), \qquad (1)$$

where $V(\sqrt{r^2 + D^2})$ is the potential energy for electron-hole pair attraction, when the electron and hole are located in two parallel monolayers separated by distance D. The Hamiltonian reflects the anisotropy of the system. In Eq. (1), m_x^e, m_y^e, m_x^h, m_y^h, $p_e^{(0)}$, and $p_h^{(0)}$ are effective constants which can be obtained from Eq. (3) using the method of completing squares as seen in Eq. (4). The constants m_x^e, m_y^e, m_x^h, and m_y^h are the effective masses of the electrons and holes in x and y. The constants $p_e^{(0)}$, and $p_h^{(0)}$ are effective constants that reflect the anisotropy of the band structure.

The low-energy $\mathbf{k}\cdot\mathbf{p}$ method applied to 1T′-MoS$_2$ yields a band structure corresponding to a model Hamiltonian that is constructed based on the symmetry properties of the valence and conduction bands. The valence and conduction bands mainly consist of d orbitals of Mo atoms and by p_y orbitals of S atoms, respectively. The notation $\lambda = \pm$ is used to distinguish the locations of two independent Dirac points. Also, $\upsilon_1 = 3.87 \times 10^5$ m/s and $\upsilon_2 = 0.46 \times 10^5$ m/s denote the Fermi velocities along the x and y directions, respectively. Additionally, $\upsilon_- = 2.86 \times 10^5$ m/s and $\upsilon_+ = 7.21 \times 10^5$ m/s are employed as velocity correction terms around the two Dirac points. The 4×4 unit matrix $\mathbf{I} = \tau_0 \otimes \sigma_0$ and Dirac matrices $\gamma_0 = \tau_1 \otimes \sigma_1$, $\gamma_1 = \tau_2 \otimes \sigma_0$, $\gamma_2 = \tau_3 \otimes \sigma_0$ are defined based on the pseudospin space $\tau_{0,1,2,3}$ and Pauli matrices $\sigma_{0,1,2,3}$. In addition, $\mathbf{k} = (k_x, k_y)$ is the wave vector, $\Delta = 0.042$ eV is the SOC gap, $\alpha = |E_z/E_c|$ is the ratio of the vertical electric field over its critical value. Taking into account the aforementioned notations, the low-energy Hamiltonian for a 2D anisotropic tilted Dirac system representing 1T′ -MoS$_2$ in the vicinity of two independent Dirac points located at (0, λ) is given by [10]

$$\hat{\mathcal{H}}_\lambda(k_x, k_y) = \hbar k_x \upsilon_1 \gamma_1 + \hbar k_y(\upsilon_2\gamma_0 - \lambda\upsilon_-\mathbf{I} - \lambda\upsilon_+\gamma_2) + \Delta(\lambda\gamma_0 - i\alpha\gamma_1\gamma_2). \qquad (2)$$

In our notation, $\xi = \pm 1$ for the conduction (valence) band, $s = \pm 1$ is the spin up (down) index, and the energy spectrum of charge carriers in 1T′-MoS$_2$ with tilted Dirac bands in the long wavelength limit near the extremum of the band structure for applied electric field not close to its critical value, $\alpha \neq 1$, is given by [9]

$$\epsilon_{\xi,s}^{\lambda}(\mathbf{k}) = \xi|\lambda - s\alpha|\Delta + [-\lambda\hbar\upsilon_- + \xi\hbar\upsilon_2 \,\mathrm{sgn}(\lambda - s\alpha)]k_y + \left(\frac{\xi\hbar^2}{2\Delta|\lambda - \alpha s|}\right)\left(\upsilon_1^2 k_x^2 + \upsilon_+^2 k_y{}^2\right), \qquad (3)$$

where $\xi = \pm 1$ for the conduction (valence) band, and $s = \pm 1$ is the spin up (down) index, and we see that it depends on both k_y (a linear term) and k_y^2 but only on a k_x^2 quadratic term. Equation (3) also shows that the spin-orbit coupling opens up a gap between spin-subbands and between the valence and conduction bands within a chosen valley. We emphasize that Eq. (3) is not valid in the gapless case. For the energy spectrum of Eq. (3), the method of completing the square is outlined below

$$\epsilon^{\lambda}_{\xi,s}(\mathbf{k}) = \xi|\lambda - s\alpha|\Delta + \left(\frac{\xi v_+^2\hbar^2}{2\Delta|\lambda-\alpha s|}\right)\times\left({k_y}^2 + \frac{[-\lambda\hbar v_- + \xi\hbar v_2\,\mathrm{sgn}(\lambda - s\alpha)](2\Delta|\lambda-\alpha s|)}{\xi v_+^2\hbar^2}k_y\right) + \left(\frac{\xi v_1^2\hbar^2}{2\Delta|\lambda-\alpha s|}\right)\left(k_x^2\right). \tag{4}$$

In Fig. 1 below, we schematically illustrate the dispersion relations of the energy bands for 1T′-MoS$_2$ as a function of the wave vector components k_x and k_y for the different excitons thoroughly discussed in Sec. II B.

From Eq. (4), we can deduce the expressions for the effective constants:

$$m_x^{e/h} = \frac{\Delta|\lambda-\alpha s|}{\xi v_1^2}, \quad m_y^{e/h} = \frac{\Delta|\lambda-\alpha s|}{\xi v_+^2}, \tag{5}$$

$$\tilde{p}^{(0)}_{e/h} = [-\lambda\hbar v_- + \xi\hbar v_2\,\mathrm{sgn}(\lambda - s\alpha)]\left(\frac{(\Delta|\lambda-\alpha s|)}{\xi v_+^2\hbar^2}\right). \tag{6}$$

It is worth noting that $p^{(0)}_{e/h}$ is a complex number, and as such the real-valued constant $\tilde{p}^{(0)}_{e/h}$ was introduced, where $p^{(0)}_{e/h} = -i\,\tilde{p}^{(0)}_{e/h}$, to easily identify complex numbers in differential equations. An extra energy term arises as a constant from Eq. (3).

A. Wave function and binding energy of an exciton

Following the procedure described in Refs. [31,32] for the separation of the relative motion of the electron-hole pair from their center-of-mass motion, one can introduce variables for the center of mass of an electron-hole pair $\mathbf{R} = (X, Y)$ and the relative motion of an electron and a hole $\mathbf{r} = (x, y)$, $X = (m_x^e x_1 + m_x^h x_2)/(m_x^e + m_x^h)$, $Y = (m_y^e y_1 + m_y^h y_2)/(m_y^e + m_y^h)$, $x = x_1 - x_2$, $y = y_1 - y_2$, and $r^2 = x^2 + y^2$.

The Schrödinger equation with Hamiltonian describing Eq. (1) has the form: $\hat{H}_0\Psi(\mathbf{r}_1, \mathbf{r}_2) = E\Psi(\mathbf{r}_1, \mathbf{r}_2)$, where $\Psi(\mathbf{r}_1, \mathbf{r}_2)$ and E are the eigenfunction and eigenenergy. One can write $\Psi(\mathbf{r}_1, \mathbf{r}_2)$ in the form $\Psi(\mathbf{r}_1, \mathbf{r}_2) = \Psi(\mathbf{R}, \mathbf{r}) = \varphi(R)\,\varphi(\mathbf{r})$, where $\varphi(\mathbf{R})$ is the wave function for the center-of-mass and $\varphi(\mathbf{r})$ is the wave function for the electron-hole pair. The wave function for the center of mass is given by the 2D Schrödinger equation:

$$\left[-\frac{\hbar^2}{2M_x}\frac{\partial^2}{\partial X^2} - \frac{\hbar^2}{2M_y}\frac{\partial^2}{\partial Y^2} - i\frac{\hbar^2}{M_y}\left(\tilde{p}^{(0)}_e + \tilde{p}^{(0)}_h\right)\frac{\partial}{\partial Y} + E_0^{(e)} + E_0^{(h)} + \eta\right]\varphi(X, Y) = \varepsilon_{\mathrm{COM}}\quad\varphi(X, Y), \tag{7}$$

where $M_x = m_x^e + m_x^h$, $M_y = m_y^e + m_y^h$, the real-valued constants $\tilde{p}^{(0)}_{e/h}$ are defined in Eq. (6), $E_0^{(e/h)}$ are spin and valley polarized constant energies that arise from Eq. (4), and η is defined in Eq. (10).

The wave function for the relative motion of the electron-hole pair is given by the 2D Schrödinger equation:

$$\left[-\frac{\hbar^2}{2\mu_x}\frac{\partial^2}{\partial x^2} - \frac{\hbar^2}{2\mu_y}\frac{\partial^2}{\partial y^2} - i\frac{\hbar^2}{\tilde{\mu}_y^*}\frac{\partial}{\partial y} + V\left(\sqrt{r^2 + D^2}\right)\right]\varphi(x, y) = \varepsilon_{\mathrm{rel}}\quad\varphi(x, y). \tag{8}$$

In Eq. (8), m_x^e, m_y^e, m_x^h, m_y^h, $p_e^{(0)}$, and $p_h^{(0)}$ are defined in Eqs. (5) and (6) and the reduced masses are defined as follows

$$\mu_{x(y)} = \frac{m^e_{x(y)}m^h_{x(y)}}{m^e_{x(y)} + m^h_{x(y)}}, \quad \tilde{\mu}_y^* = \frac{m_y^e m_y^h}{m_y^e\tilde{p}_h^{(0)} + m_y^h\tilde{p}_e^{(0)}}, \tag{9}$$

$$\eta = \frac{\hbar^2}{2}\frac{m_y^e\tilde{p}_h^{(0)2} + m_y^h\tilde{p}_e^{(0)2}}{m_y^e m_y^h}. \tag{10}$$

It is worth noting that η is a positive, real number and we introduce the real-valued constant $\tilde{\mu}_y^*$ to easily identify complex numbers in equations. The potential energy of the electron-hole attraction in this system is described by the Coulomb potential [36], $V(r) = -e^2/(4\pi\varepsilon_0\epsilon_d r_{eh})$, where $\varepsilon_0 = 8.85\times10^{-12}$ C^2 N^{-1} m^{-2} is the permitivity of free space, and ϵ_d is the background dielectric constant, which for our chosen dielectric, h-BN has a numerical value of 4.89 [20]. Making use of $r_{eh} = \sqrt{r^2 + D^2}$, where r_{eh} is the distance between the electron and hole located in different parallel planes, and assuming $r \ll D$, one can expand the potential as a Taylor series in terms of $(r/D)^2$. By limiting ourselves to the first order with respect to $(r/D)^2$, we obtain

$$V(r) = -V_0 + \gamma r^2. \tag{11}$$

Assuming $r \ll D$ and retaining only the first two terms of the Taylor series, one obtains the following expressions for V_0 and γ:

$$V_0 = \frac{e^2}{4\pi\varepsilon_0\epsilon_d D}, \qquad \gamma = \frac{e^2}{8\pi\varepsilon_0\epsilon_d D^3}. \tag{12}$$

Replacement of $V(\sqrt{r^2 + D^2})$ by the potential in Eq. (11) allows one to reduce the problem of indirect exciton formed between two layers to an exactly solvable two-body problem as this is demonstrated in this section. Substituting Eq. (11) with parameters in Eq. (12) for the Coulomb potential, and using $r^2 = x^2 + y^2$, one obtains an equation which has the form of the Schrödinger equation for a 2D anisotropic harmonic oscillator. This allows us to carry out separation of variables to obtain two independent equations

$$-\frac{\hbar^2}{2\mu_x}\frac{\partial^2}{\partial x^2}\psi(x) + \gamma x^2\psi(x) = \left(\varepsilon_x + \frac{V_0}{2}\right)\psi(x), \tag{13}$$

$$-\frac{\hbar^2}{2\mu_y}\frac{\partial^2}{\partial y^2}\psi(y) - \frac{\hbar^2}{\tilde{\mu}_y^*}\frac{\partial}{\partial y}\psi(y) + \gamma y^2\psi(y) = \left(\varepsilon_y + \frac{V_0}{2}\right)\psi(y). \tag{14}$$

The wave function and eigenenergies of Eq. (13) are obtained simply since it is the well-studied solution to a 1D harmonic oscillator. The process for solving Eq. (14) is the following. First, we assume that $\psi(y)$ has the form of two

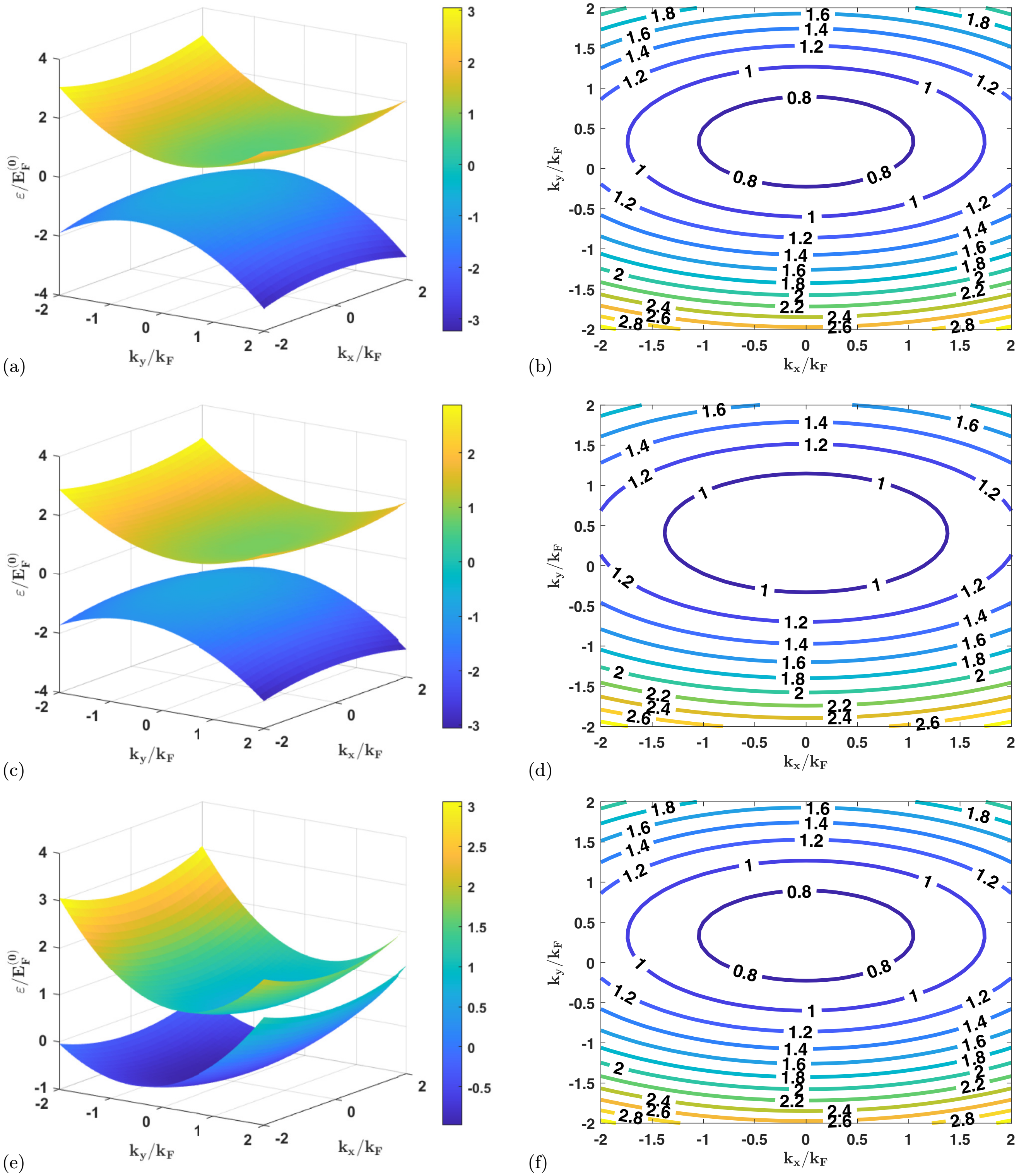

FIG. 1. Schematic illustrations of the energy bands of the charge carriers, forming the different types of excitons defined in Sec. II B, with $\alpha = 0.1$. (a), (c), and (e) represent 3D plots of the energy bands for the charge carriers, forming type A, B, and C excitons, respectively. Additionally, (b), (d), and (f) represent contour plots of the conduction band charge carriers, forming type A, B, and C excitons, respectively. The plots are labeled with the unitless energy scaled by the Fermi energy, of $E_F^{(0)} = 52.02$ meV. The wave vector is expressed in terms of the Fermi momentum $k_F = 7.92 \times 10^{-7}$ m^{-1}.

functions multiplied as seen below

$$\psi(y) = f(y) \cdot g(y), \tag{15}$$

allowing us to rewrite Eq. (14) in the following form:

$$\begin{aligned} &a_2 g(y) \frac{\partial^2}{\partial y^2} f(y) + \left(2a_2 \frac{\partial}{\partial y} g(y) - i\tilde{a}_1 g(y) \right) \frac{\partial}{\partial y} f(y) \\ &\quad + \left(a_2 \frac{\partial^2}{\partial y^2} g(y) - i\tilde{a}_1 \frac{\partial}{\partial y} g(y) + (\gamma y^2 - E_y) g(y) \right) f(y) = 0, \end{aligned} \tag{16}$$

where

$$E_y = \varepsilon_y + \frac{V_0}{2}, \quad a_2 = -\frac{\hbar^2}{2\mu_y}, \quad \tilde{a}_1 = \frac{\hbar^2}{\tilde{\mu}_y^*}. \tag{17}$$

By imposing the condition that the coefficient of the first derivative of $f(y)$ in Eq. (16) must be equal to zero, we find the form of $g(y)$.

$$2a_2 \frac{\partial}{\partial y} g(y) - i\tilde{a}_1 g(y) = 0, \quad g(y) = F e^{i\frac{\tilde{a}_1 y}{2a_2}}, \tag{18}$$

where F is an undetermined constant. Inserting our result from Eq. (18) into Eq. (16) we obtain an equation that determines $f(y)$. This equation is of the form for a 1D harmonic oscillator, i.e.,

$$a_2 \frac{\partial^2}{\partial y^2} f(y) + \gamma y^2 f(y) = \left(E_y - \frac{\tilde{a}_1^2}{4a_2} \right) f(y). \tag{19}$$

Using the condition of normalization $\int_{-\infty}^{\infty} |\psi(y)|^2 \, dy = 1$ we find $F = 1$. The normalized eigenfunctions for Eqs. (13) and (14) are given by

$$\psi_n(x) = \frac{1}{\pi^{1/4} a_x^{1/2}} \frac{1}{\sqrt{2^n n!}} e^{-x^2/\left(2a_x^2\right)} H_n\left(\frac{x}{a_x}\right), \tag{20}$$

$$\psi_m(y) = e^{-i\frac{\mu_y y}{\tilde{\mu}_y^*}} \frac{1}{\pi^{1/4} a_y^{1/2}} \frac{1}{\sqrt{2^m m!}} e^{-y^2/\left(2a_y^2\right)} H_m\left(\frac{y}{a_y}\right), \tag{21}$$

where $n, m = 0, 1, 2, 3, \ldots$ are quantum numbers, $H_n(\frac{x}{a_x})$, and $H_m(\frac{y}{a_y})$ are Hermite polynomials, and $a_x = (\hbar/(\sqrt{2\mu_x \gamma})^{1/2}$ and $a_y = (\hbar/(\sqrt{2\mu_y \gamma})^{1/2}$.

The overarching wave function for the relative motion of the electron-hole pair in Eq. (8) is thus given by $\psi_{n,m}(x, y) = \psi_n(x)\psi_m(y)$. The corresponding eigenenergies are

$$\begin{aligned} \varepsilon_n^{(x)} &= -\frac{V_0}{2} + \hbar\sqrt{\frac{2\gamma}{\mu_x}}(n + 1/2), \\ \varepsilon_m^{(y)} &= -\frac{V_0}{2} + \hbar\sqrt{\frac{2\gamma}{\mu_y}}(m + 1/2) - \frac{\hbar^2 \mu_y}{2\tilde{\mu}_y^{*2}}. \end{aligned} \tag{22}$$

The total eigenergy of the relative motion of the electron-hole pair can be expressed as

$$\varepsilon_{nm} = \varepsilon_n^{(x)} + \varepsilon_m^{(y)}, \tag{23}$$

where $n, m = 0, 1, 2, 3, \ldots$

The variables X and Y in the Schrödinger equation for the center-of-mass can be separated in Eq. (7) to obtain the following equations:

$$\left[-\frac{\hbar^2}{2M_x} \frac{\partial^2}{\partial X^2} \right] \phi(X) = \varepsilon_X \phi(X), \tag{24}$$

$$\left[-\frac{\hbar^2}{2M_y} \frac{\partial^2}{\partial Y^2} - i\frac{\hbar^2}{M_y} \left(\tilde{p}_e^{(0)} + \tilde{p}_h^{(0)} \right) \frac{\partial}{\partial Y} \right] \phi(Y) = \varepsilon_Y \phi(Y), \tag{25}$$

where $M_X = m_x^e + m_x^h$, and $M_Y = m_y^e + m_y^h$. We will also be employing the notation $\tau = \tilde{p}_e^{(0)} + \tilde{p}_h^{(0)}$ for convenience. The equation for the center of mass in X, Eq. (24), is simply that of a free particle. The solutions of Eqs. (24) and (25), $\phi(X)$ and $\phi(Y)$ are given by

$$\phi(X) = \frac{1}{\sqrt{L_X}} e^{i\frac{P_X}{\hbar} X}, \quad \phi(Y) = \frac{1}{\sqrt{L_Y}} e^{i\left(\frac{P_Y}{\hbar} - \tau\right) Y}. \tag{26}$$

The center-of-mass eigenenergies ε_X and ε_Y are given by

$$\varepsilon_X = \frac{P_X^2}{2M_X}, \quad \varepsilon_Y = \frac{P_Y^2}{2M_Y} - \frac{\hbar^2 \tau^2}{2M_Y}. \tag{27}$$

The total eigenfunction and eigenergy for the center-of-mass equation are given by

$$\begin{aligned} &\phi(X, Y) = \phi(X)\phi(Y), \\ &\qquad \varepsilon_{\text{COM}} = \varepsilon_X + \varepsilon_Y + E_0^{(e)} + E_0^{(h)} + \eta. \end{aligned} \tag{28}$$

B. Types of excitons and tunability of parameters

The effects due to mass anisotropy on the exciton binding energy have been demonstrated in previous work [33]. The location of the electron (hole) in the vicinity of two inequivalent valleys K and K' is characterized by its Dirac point (this is represented by the valley index $\lambda_{e(h)} = \pm 1$, where a particle index has been added as subscript e, h). The effective mass of the electron (hole) is also spin dependent, and is designated by the spin index $s_{e(h)} = \pm 1$ with appropriate subscripted indices. The valley index, along with the particle's spin, determines the effective masses of the electron and hole, and also the effective mass of the excitons. Using different combinations of these two parameters, we are able to categorize the excitons by three types, with each type having a different reduced mass. The first type of exciton arises when the sign of the valley index has the same sign as the spin of the electron ($\lambda_e = \lambda_h = s_e$). We refer to these as "type A" excitons. The second type of exciton occurs when the sign of the valley index is opposite the sign of the spin of the electron ($\lambda_e = \lambda_h = -s_e$). We term these "type B" excitons. It is important to note that the spin of the hole, when computed, is opposite that of the electron state being annihilated. These types of excitons can be formed by employing circularly polarized light. Table I presents these combinations of excitons induced by circularly polarized light, and outlines the effective masses of the electron and hole along the x and y directions. Table II presents the combinations of excitons induced by linearly polarized light. These excitons allow for electrons and holes of different spins to exist in two different valleys. These are designated by the signs of the valley index ($\lambda_e = -\lambda_h$).

TABLE I. Combinations of $\lambda_{e(h)}$ and assorted spins $s_{e(h)}$ for type A and B excitons and their respective effective masses. The first two rows designate the properties and effective masses of electrons and holes for type A excitons, and the last two rows designate the properties and effective masses of electrons and holes for type B excitons. In this notation, $s_{e(h)} = \pm 1$ is the spin up (down) index, and $\lambda_{e(h)} = \pm$ is used to distinguish the locations of two independent Dirac points.

λ_e	λ_h	s_e	s_h	m_x^e	m_x^h	m_y^e	m_y^h
+	+	+	-	$\frac{\Delta\|1-\alpha\|}{\xi v_1^2}$	$\frac{\Delta\|1-\alpha\|}{\xi v_1^2}$	$\frac{\Delta\|1-\alpha\|}{\xi v_p^2}$	$\frac{\Delta\|1-\alpha\|}{\xi v_p^2}$
-	-	-	+	$\frac{\Delta\|1-\alpha\|}{\xi v_1^2}$	$\frac{\Delta\|1-\alpha\|}{\xi v_1^2}$	$\frac{\Delta\|1-\alpha\|}{\xi v_p^2}$	$\frac{\Delta\|1-\alpha\|}{\xi v_p^2}$
+	+	-	+	$\frac{\Delta\|1+\alpha\|}{\xi v_1^2}$	$\frac{\Delta\|1+\alpha\|}{\xi v_1^2}$	$\frac{\Delta\|1+\alpha\|}{\xi v_p^2}$	$\frac{\Delta\|1+\alpha\|}{\xi v_p^2}$
-	-	+	-	$\frac{\Delta\|1+\alpha\|}{\xi v_1^2}$	$\frac{\Delta\|1+\alpha\|}{\xi v_1^2}$	$\frac{\Delta\|1+\alpha\|}{\xi v_p^2}$	$\frac{\Delta\|1+\alpha\|}{\xi v_p^2}$

We shall refer to these as "type C" excitons. Using the data outlined in Tables I and II, we are able to then calculate the effective masses in terms of the mass of a free electron (m_0), and proceed to represent them graphically as functions of α, seen below in Fig. 1.

Figure 1 shows schematic representations of the energy dispersion bands for the charge carriers that form the different types of excitons. The bands are shifted semi-Dirac cones. The difference in band curvature near the origin between different types of excitons comes from the fact that various types of excitons are characterized by different effective masses. The curvature also depends on the chosen values of α, the scaled external perpendicular electric field. We can find such values of α which correspond to higher exciton binding energy implying more stable excitons. Figure 1 also demonstrates the anisotropy of our system which forms the basis for the directional indirect momentum space dark exciton superfluidity presented in Secs. IV and V. The relationship between the reduced masses and total masses for other excitons depends on both the chosen spin and valley. We will also see the out-of-plane electric field, α can be used to tune the exciton binding energies, by tuning the effective mass parameters [10,34]. Specifically, for the three types of excitons, we see different behavior. For type A excitons, we observe that both the reduced mass and that for the total mass decrease linearly from $0 \leqslant \alpha \leqslant 1.0$ with an increase of α, while for $\alpha \geqslant 1$, the reduced mass and that for the total mass increase linearly with an increase of α. For type B excitons, the reduced mass and that for the total mass increase linearly for all α, with increase of α. Notably, for both type A and type B excitons, the reduced mass in **x** (μ_x) and total mass in **X** (M_X), are larger than the reduced mass in **y** (μ_y) and total mass in **Y** (M_Y).

TABLE II. Combinations of $\lambda_{e(h)}$ and assorted spins $s_{e(h)}$ for type C excitons and their respective masses. In this notation, $s_{e(h)} = \pm 1$ is the spin up (down) index, and $\lambda_{e(h)} = \pm$ is used to distinguish the locations of two independent Dirac points.

λ_e	λ_h	s_e	s_h	m_x^e	m_x^h	m_y^e	m_y^h
+	-	+	-	$\frac{\Delta\|1-\alpha\|}{\xi v_1^2}$	$\frac{\Delta\|1+\alpha\|}{\xi v_1^2}$	$\frac{\Delta\|1-\alpha\|}{\xi v_p^2}$	$\frac{\Delta\|1+\alpha\|}{\xi v_p^2}$
+	-	-	+	$\frac{\Delta\|1+\alpha\|}{\xi v_1^2}$	$\frac{\Delta\|1-\alpha\|}{\xi v_1^2}$	$\frac{\Delta\|1+\alpha\|}{\xi v_p^2}$	$\frac{\Delta\|1-\alpha\|}{\xi v_p^2}$
-	+	+	-	$\frac{\Delta\|1+\alpha\|}{\xi v_1^2}$	$\frac{\Delta\|1-\alpha\|}{\xi v_1^2}$	$\frac{\Delta\|1+\alpha\|}{\xi v_p^2}$	$\frac{\Delta\|1-\alpha\|}{\xi v_p^2}$
-	+	-	+	$\frac{\Delta\|1-\alpha\|}{\xi v_1^2}$	$\frac{\Delta\|1+\alpha\|}{\xi v_1^2}$	$\frac{\Delta\|1-\alpha\|}{\xi v_p^2}$	$\frac{\Delta\|1+\alpha\|}{\xi v_p^2}$

For type C excitons, we observe similar behaviour, seen above in Fig. 2. The reduced mass decreases nonlinearly from $0 \leqslant \alpha \leqslant 1$ and increases nonlinearly for $\alpha \geqslant 1$. The total mass is constant for $0 \leqslant \alpha \leqslant 1$ and increases linearly for $\alpha \geqslant 1$, with increasing α. Based on these results we can conclude that using a large value of α is beneficial for our binding energies, since it leads to larger values of binding energies, thus increasing the stability of the excitons.

C. Binding Energy of excitons with *h*-BN dielectric

The binding energy corresponding to the energy spectrum of an electron and hole described by Eq. (23), is given by

$$E_B = -\mathcal{E}_{00} = V_0 - \hbar\sqrt{\frac{\gamma}{2\mu_x}} - \hbar\sqrt{\frac{\gamma}{2\mu_y}} = V_0 - \hbar\sqrt{\frac{\gamma}{2\mu_0}}, \quad (29)$$

where E_B is the dipolar exciton binding energy, defined as the negative of the eigenenergy defined in Eq. (23), calculated at $n = 0$, $m = 0$. In Eq. (29), we define the quantity $\mu_0 = \frac{\mu_x \mu_y}{(\sqrt{\mu_x} + \sqrt{\mu_y})^2}$ for convenience. In Fig. 3, we note that the binding energy of type A excitons is decreased for increasing D with chosen α, and is increased for increasing α, for chosen D. In our structure, we have thin sheets of h-BN dielectric between layers and occupy the interlayer region of separation D. The dielectric is inserted to reduce degradation of the heterostructure and reduce the photoluminescence linewidth (PL) [35]. Each layer of h-BN is 0.33 nm thick and as such for experimental considerations, we restrict the number of layers to ten, or fewer, so as to be experimentally viable, while also forming a bound state of the exciton. Consequently, a desirable choice of parameters for the system includes a large binding energy, comparable in magnitude to prior results [22], and a low interlayer separation D about 3.3 nm. We find that for larger values of α, we can obtain larger binding energy for $D = 20.0$ nm which corresponds to a value of $\alpha = 6.0$. For all of type A, B, C excitons, the choice of $\alpha = 6.0$ or higher, allows for larger binding energy with a desirably low interlayer separation. We see that the larger the reduced mass, the greater the binding energy, as per our theoretical predictions. Too large an interlayer separation is not desirable since that would require a very large number of layers of h-BN dielectric.

For each type of our excitons (type A, B, C), we find that a larger value of α satisfies the criteria for a small interlayer separation D, with a growing value of the binding energy, which is preferable for stability of the exciton. This behavior is illustrated in Figs. 3–6. When $\alpha = 35.0$, we find that the binding energy of type A, B, and C excitons is 33.9, 35.5, and 34.7 meV, respectively, for an interlayer separation of $D = 3.3$ nm, which corresponds to $N_L = 10$ layers of *h*-BN. It is worth noting that the corresponding value of D_0 for type A, B, and C excitons is 0.63, 0.59, and 0.62 nm, respectively. Consequently, the first-order Taylor series expansion is valid for the Coulomb potential. These results are as expected based on prior results [36].

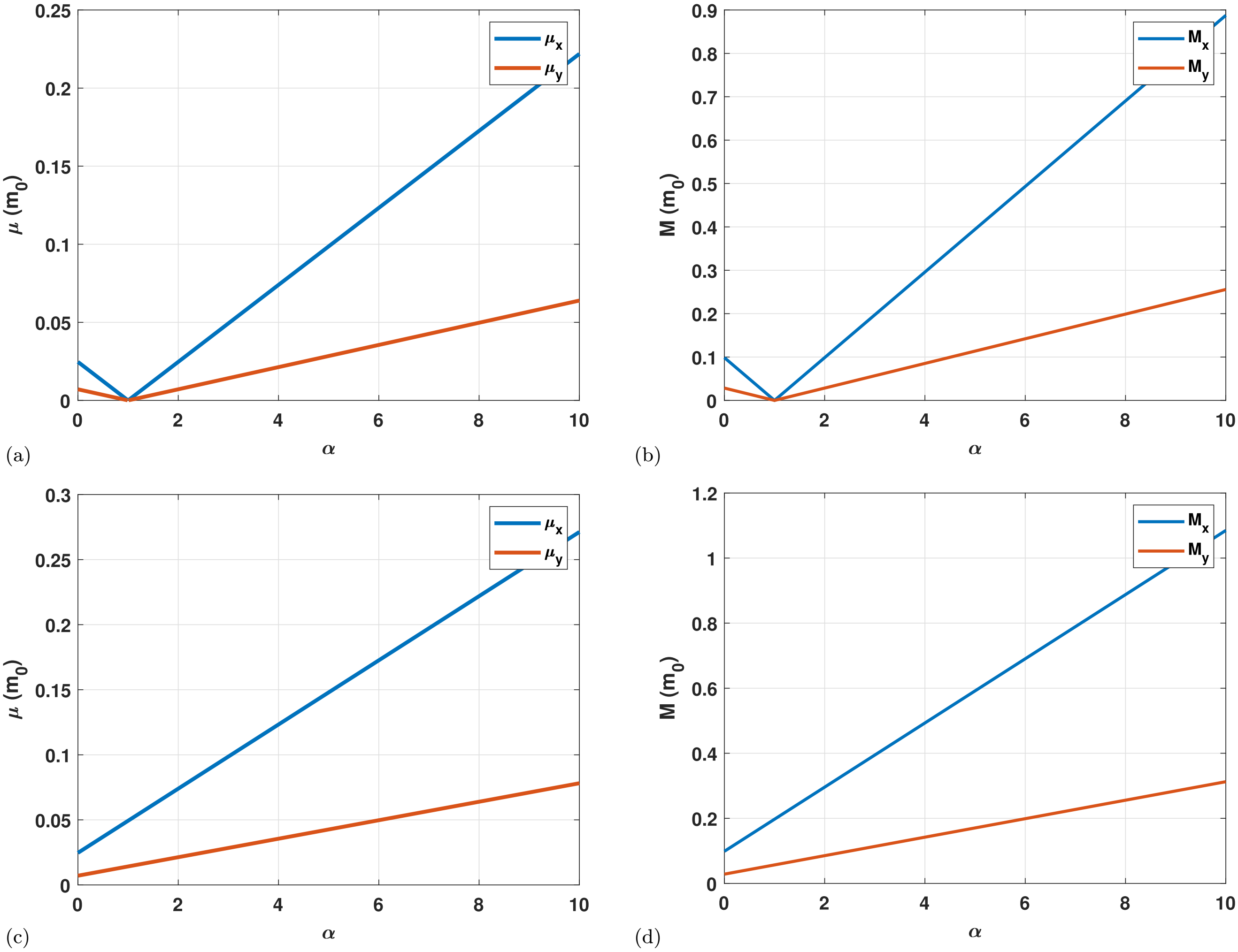

FIG. 2. (a) The reduced mass of type A excitons as a function of α, (b) total mass of type A excitons, (c) the reduced mass of type B excitons and (d) total mass of type B excitons vs α. We employed the effective mass defined in Eq. (9) for generating these plots. The results are scaled by m_0, the free electron mass.

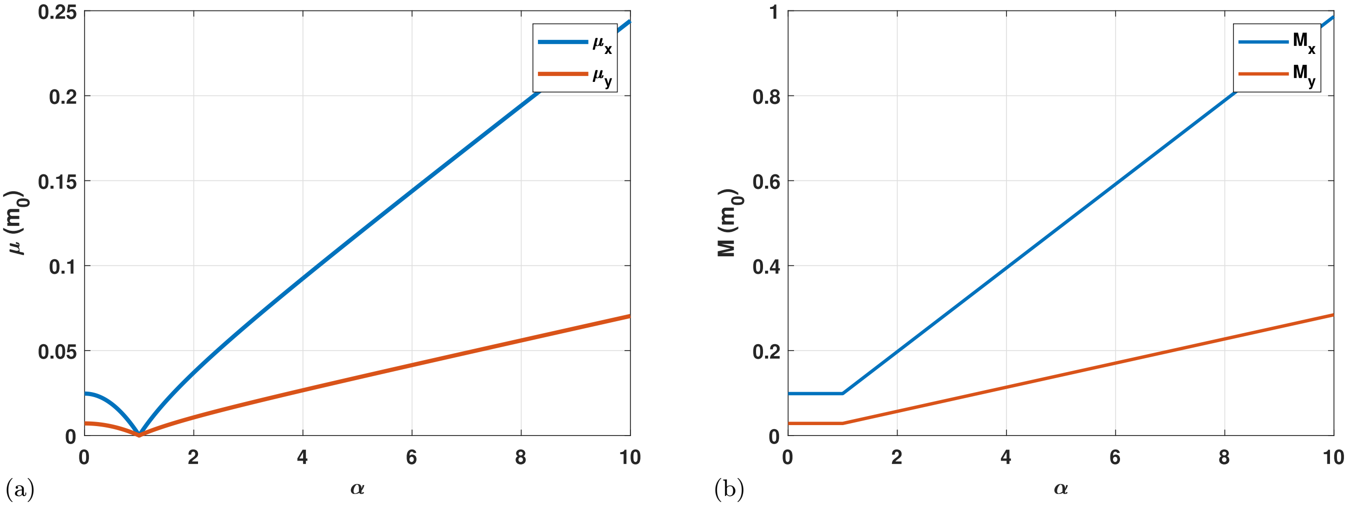

FIG. 3. (a) The reduced mass for type C excitons vs α. In (b), the total exciton mass of type C exciton is also plotted as a function of the scaled perpendicular electric field. We employed the definition of the effective mass definitions of Eq. (9) in these calculations.

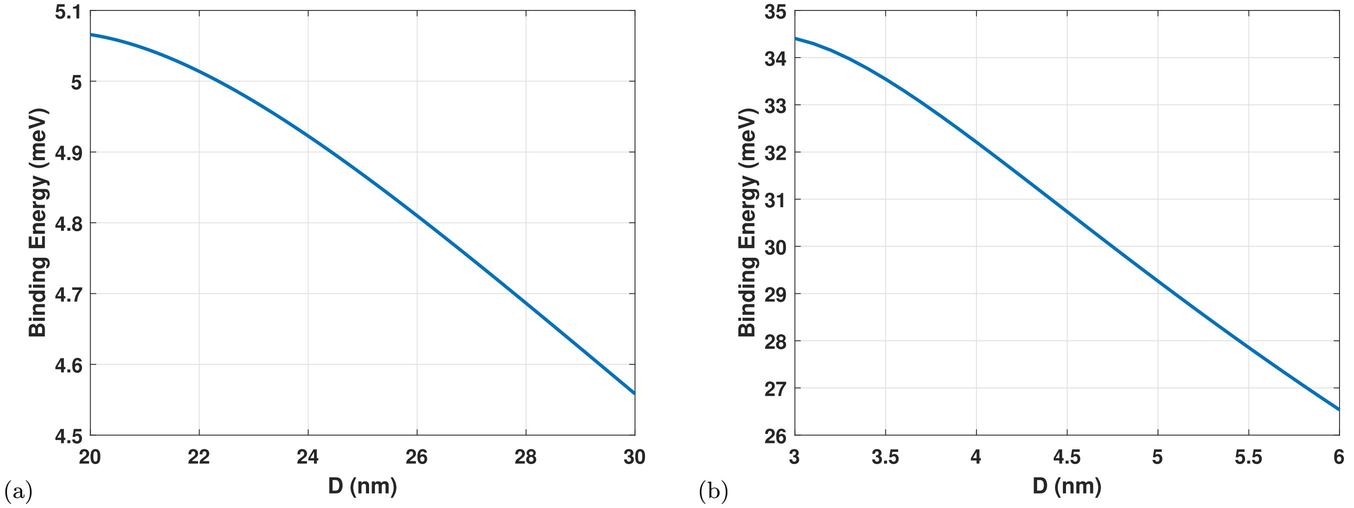

FIG. 4. The binding energy of type A excitons as a function of the interlayer separation D for chosen perpendicular electric field with (a) $\alpha = 6.0$ and (b) 35.0. We employed the binding energy definition in Eq. (29), along with the effective mass definitions given in Eqs. (11)– (15) for generating of these figures.

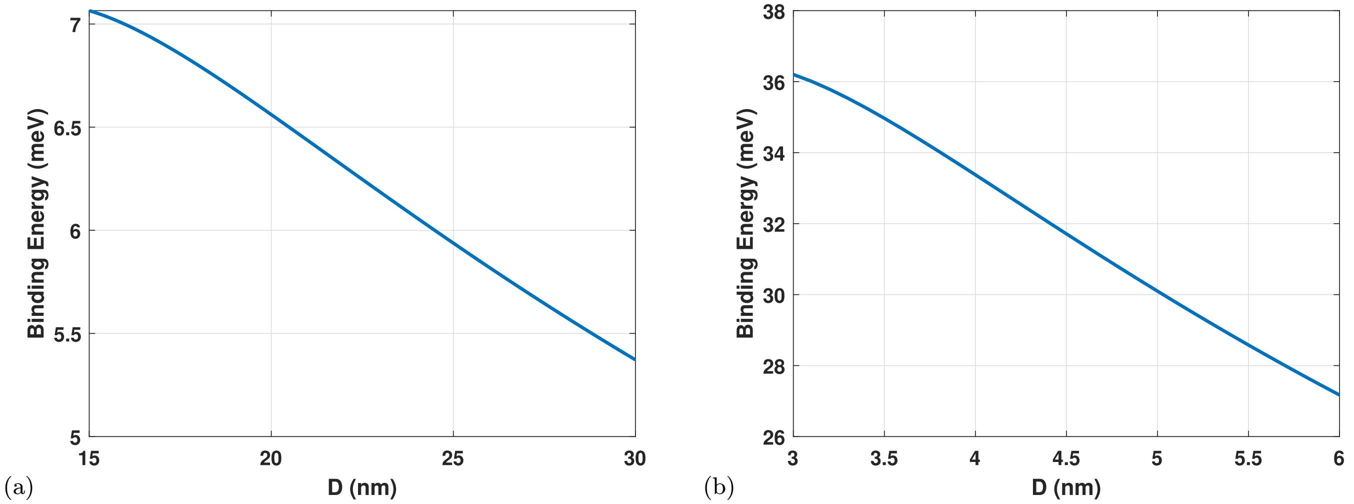

FIG. 5. Plot of the binding energy for type B excitons as a function of the interlayer separation D for chosen perpendicular electric field. (a) $\alpha = 6.0$ and (b) 35.0. We employed the binding energy definitined in Eq. (29), along with the effective mass definitions of Eq. (9) in the calculations for these figures.

III. COLLECTIVE EXCITATIONS FOR SPATIALLY SEPARATED ELECTRONS AND HOLES

In this section, we examine the dilute limit for gases of electrons and holes in a double layer of 1T$'$-MoS$_2$. In this limit, we consider dipolar type A and type B excitons. However, the analysis holds true for all other combinations of types of excitons, i.e., type A and type C, and type B and type C. Henceforth, we will refer to type A, B, and C excitons, simply as A, B, and C excitons for brevity. In this section, we formulate the sound velocity, which will determine whether the Landau criterion for superfluidity is satisfied.

We expect that at $T = 0$ K almost all A and B excitons condense into a BEC of A and B excitons. This allows us to assume the formation of a binary mixture of BECs. We will describe this two-component weakly interacting Bose gas of excitons following the procedure, described in Refs. [21,22,37]. We then examine this mixture within the Bogoliubov approximation [38]. Only the interactions between the condensate and noncondensate particles are considered, since we assume almost all the particles belong to the BEC. The interactions between noncondensate particles are neglected. This allows us to diagnolize the many particle Hamiltonian. This reduces the product of four operators in the interaction term of the Hamiltonian by replacing it with a pair consisting of a product of two operators [39]. The condensate operators are replaced by numbers, and the resulting Hamiltonian is quadratic with respect to the creation and annihilation operators. Employing the Bogoliubov approximation [39], generalized for a two-component weakly interacting Bose gas, we obtain the chemical potential μ of the excitonic system by minimizing $\hat{H}_0 - \mu\hat{N}$ with respect to the 2D concentration n

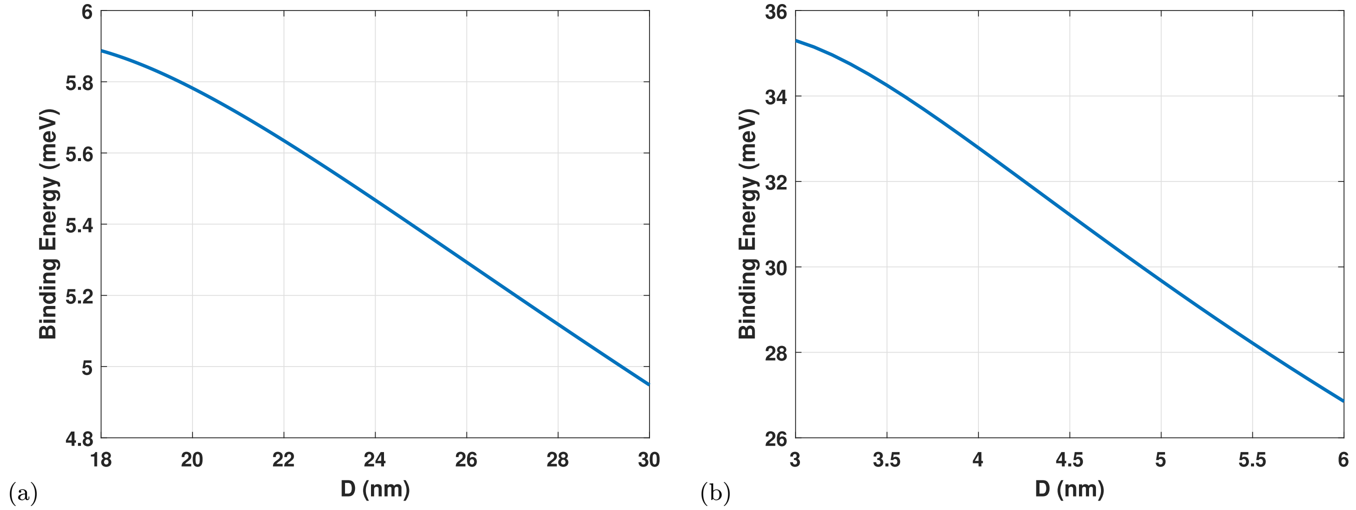

FIG. 6. Relationship between the binding energy of type **C** excitons and the interlayer separation D, at different values of α: (a) 6.0 and (b) 35.0. We employed the binding energy definition of Eq. (29), along with the effective mass definitions of Eq. (9), in the generation of these figures.

[40], where $\hat{N}$ denotes the number operator

$$\hat{N} = \sum_{\mathbf{P}} a^{\dagger}_{\mathbf{p}A} a_{\mathbf{p}A} + \sum_{\mathbf{P}} a^{\dagger}_{\mathbf{p}B} a_{\mathbf{p}B}, \tag{30}$$

and H_0 is the Hamiltonian describing the particles in the condensate with zero momentum $\mathbf{p} = 0$. In the Bogoliubov approximation, we assume $N = N_0$, $a^{\dagger}_{\mathbf{p}=0A(B)} = \sqrt{N_{0A(B)}}e^{-i\Theta_{A(B)}}$, and $a_{\mathbf{p}=0,A(B)} = \sqrt{N_{0A(B)}}e^{i\Theta_{A(B)}}$, where N is the total number of all excitons in the condensate, $N_{0A(B)}$ and $\Theta_{A(B)}$ are the number and phase for $A(B)$ excitons in the condensate. Following the standard procedure for calculations outlined in Sec. II of Ref. [28], we obtain the spectrum of collective excitations $\varepsilon_j(P, \Theta)$

$$\varepsilon_j(P, \Theta) = \sqrt{\frac{\omega_A^2(P, \Theta) + \omega_B^2(P, \Theta) + (-1)^{j-1}\sqrt{\left[\omega_A^2(P, \Theta) - \omega_B^2(P, \Theta)\right]^2 + 4g^2n^2\varepsilon_{(0)A}(P, \Theta)\varepsilon_{(0)B}(P, \Theta)}}{2}}. \tag{31}$$

In the small momentum limit, $p = \hbar k$ when $\varepsilon_{(0)A}(P, \Theta) \ll G_{AA}$, and $\varepsilon_{(0)B}(P, \Theta) \ll G_{BB}$ we expand the spectrum of collective excitations $\varepsilon_j(p, \Theta)$ up to first order with respect to the momentum p and obtain two sound modes of the collective excitations $\varepsilon_j(p, \Theta) = c_j(\Theta)p$, where $c_j(\Theta)$ is the sound velocity given by

$$c_j(\Theta) = \sqrt{\frac{G_{AA}}{2M_{0A}(\Theta)} + \frac{G_{BB}}{2M_{0B}(\Theta)} + (-1)^{j-1}\sqrt{\left(\frac{G_{AA}}{2M_{0A}(\Theta)} - \frac{G_{BB}}{2M_{0B}(\Theta)}\right)^2 + \frac{G_{AB}^2}{M_A(\Theta)M_B(\Theta)}}}, \tag{32}$$

where $j = 1, 2$, and G_{AA}, G_{BB}, and G_{AB} are exciton-exciton coupling constant g multiplied by the 2D concentration of A and B excitons, n_A, n_B, and $\sqrt{n_A n_B}$, respectively. These are defined formally below in Eqs. (33) and (34)

$$g = \frac{4\pi k e^2 D^2 \sqrt{\pi n}}{\epsilon_d}, \tag{33}$$

$$G_{AA} = g_{AA}n_A = gn_A,\ G_{BB} = g_{BB}n_B = gn_B,$$
$$G_{AB} = g_{AB}\sqrt{n_A n_B} = g\sqrt{n_A n_B}. \tag{34}$$

By employing the method presented in Refs. [21,22,41,42], the interaction parameters for the exciton-exciton interaction in a very dilute system were obtained. We assume that the potential energy of the exciton-exciton dipole-dipole repulsion equals to a nonzero constant only at the distances between the excitons less than the distance from an exciton to the classical turning point. If the distance between two excitons is greater than the distance from an exciton to the classical turning point, the potential energy of the interaction between two excitons is zero. This distance from an exciton to the classical turning point is determined by the conditions reflecting the fact that the energy of two excitons, separated at the distance equal to the distance from an exciton to the classical turning point, equals twice the chemical potential of the system [21,22,41,42]. Details of these standard calculations can be obtained in Ref. [28].

Upon making use of Eqs. (33) and (34) in Eq. (32), calculation shows that when $j = 2$ the sound velocity vanishes when $c_2(\Theta) = 0$, whereas when $j = 1$ the spectrum of collective excitations is determined by the nonzero sound velocity $c_1(\Theta)$. Detailed calculations are presented in Ref. [28]. In the large momentum limit when $\varepsilon_{(0)A}(P, \Theta) \gg G_{AA}$, and

$\varepsilon_{(0)B}(P,\Theta) \gg G_{BB}$, we get two parabolic modes of collective excitations with the spectra $\varepsilon_1(p,\Theta) = \varepsilon_{(0)A}(p,\Theta)$ and $\varepsilon_2(p,\Theta) = \varepsilon_{(0)B}(p,\Theta)$. The Hamiltonian $\hat{H}_{\rm col}$ of collective excitations, corresponding to two branches of the spectrum, in the Bogoliubov approximation for the entire two-component anisotropic system is given by

$$\hat{H}_{\rm col} = \sum_{\mathbf{P}\neq 0} \varepsilon_1(P,\Theta)\alpha^{\dagger}_{1\mathbf{p}}\alpha_{1\mathbf{p}} + \sum_{\mathbf{P}\neq 0} \varepsilon_2(P,\Theta)\alpha^{\dagger}_{2\mathbf{p}}\alpha_{2\mathbf{p}}, \quad (35)$$

where $\alpha^{\dagger}_{j\mathbf{P}}$ and $\alpha_{j\mathbf{P}}$ are the creation and annihilation Bose operators for the quasiparticles with the energy dispersion corresponding to the jth mode of the spectrum of the collective excitations. For simplicity, we consider the specific case when the concentrations of A and B excitons are the same as $n_A = n_B = n/2$. Thus we can obtain the sound velocity at $n_A = n_B = n/2$ as

$$c_j(\Theta) = \sqrt{\frac{gn}{2}\left(\frac{1}{2M_{0A}(\Theta)} + \frac{1}{2M_{0B}(\Theta)} + (-1)^{j-1}\sqrt{\left(\frac{1}{2M_{0A}(\Theta)} - \frac{1}{2M_{0B}(\Theta)}\right)^2 + \frac{1}{M_{0A}(\Theta)M_{0B}(\Theta)}}\right)}. \quad (36)$$

It follows from Eq. (36) that there is only one nonzero sound velocity at $n_A = n_B = n/2$ given by

$$c_S(\Theta) = \sqrt{\frac{gn}{2}\left(\frac{1}{M_{0A}(\Theta)} + \frac{1}{M_{0B}(\Theta)}\right)}. \quad (37)$$

It is also worth noting that the large interlayer separation D, between the double layer allows us to neglect the exchange interactions in the electron-hole system. This is caused by a low tunneling probability caused by the shielding of the dipole-dipole interaction by the dielectric (h-BN) that separates the layers in the double layer [21].

IV. SUPERFLUIDITY

In this section, we determine the criterion for which a weakly interacting Bose gas of dipolar excitons can form a superfluid. Since at low momenta the energy spectrum of quasiparticles of a weakly interacting gas of excitons is soundlike, this system satisfies the Landau criterion for superfluidity [39]. The critical velocity for superfluidity is given by $v_c = \min(c_1(\Theta), c_2(\Theta))$ since the quasiparticles are created at velocities exceeding that of sound for the lowest mode of the quasiparticle dispersion. Additionally, it is angular dependent. The density of the superfluid $\rho_s(T)$ is defined as $\rho_s(T) = \rho - \rho_n(T)$, where $\rho = M_A n_A + M_B n_B$, is the total 2D density of the system and $\rho_n(T)$ is the density of the normal component. We define the normal component $\rho_n(T)$ in the usual way [41]. Assume that the excitonic system moves with velocity $\mathbf{u}$, which means that the superfluid component has velocity $\mathbf{u}$. At finite temperatures T, dissipating quasiparticles will emerge in this system. Since their density is small at low temperatures, one may assume that the gas of quasiparticles is an ideal Bose gas. We will obtain the density of the superfluid component in the anisotropic system following the procedure, described in Ref. [42]. To calculate the superfluid component density, we begin by defining the mass current $\mathbf{J}$ for a Bose gas for quasiparticles in the frame of reference where the superfluid component is at rest by

$$\mathbf{J} = s\int \frac{d^2P}{(2\pi\hbar)^2}\mathbf{P}[f[\varepsilon_1(P,\Theta) - \mathbf{Pu}] + f[\varepsilon_2(P,\Theta) - \mathbf{P}\cdot\mathbf{u}]], \quad (38)$$

where $f[\varepsilon_1(P,\Theta)] = \{\exp[\varepsilon_1(P,\Theta)/(k_BT)] - 1\}^{-1}$ and $f[\varepsilon_2(P,\Theta)] = \{\exp[\varepsilon_2(P,\Theta)/(k_BT)] - 1\}^{-1}$ are the Bose-Einstein distribution functions for the quasiparticles with the angle dependent dispersions $\varepsilon_1(P,\Theta)$ and $\varepsilon_2(P,\Theta)$ respectively, s is the spin degeneracy factor, and k_B is the Boltzmann constant. Expanding the expression under the integral in terms of $\mathbf{Pu}/k_BT$ and restricting ourselves to the first-order term, we obtain

$$\mathbf{J} = -\frac{s}{k_BT}\int \frac{d^2P}{(2\pi\hbar)^2}\mathbf{P}(\mathbf{P}\cdot\mathbf{u})\left(\frac{\partial f[\varepsilon_1(P,\Theta)]}{\partial\varepsilon_1(P,\Theta)} + \frac{\partial f[\varepsilon_2(P,\Theta)]}{\partial\varepsilon_2(P,\Theta)}\right). \quad (39)$$

The normal density ρ_n in the anisotropic system takes tensor form. We define the tensor elements for the normal component density $\rho_n^{(ij)}(T)$ by

$$J_i = \rho_n^{(ij)}(T)u_j, \quad (40)$$

where i, j denote either x, y component. Assuming that the vector $\mathbf{u}$ is parallel to the OX axis and has the same direction as this axis, we have $\mathbf{u} = u_x\mathbf{i}$ and $\mathbf{P} = P_x\mathbf{i} + P_y\mathbf{j}$ and $\mathbf{P}\cdot\mathbf{u} = P_xu_x$, $\mathbf{P}(\mathbf{P}\cdot\mathbf{u}) = P_x^2u_x\mathbf{i} + P_xP_yu_x\mathbf{j}$, where $\mathbf{i}$ and $\mathbf{j}$ are unit vectors in the x and y directions, respectively. We then obtain

$$J_x = -\frac{s}{k_BT}\int_0^{\infty} dP\frac{P^3}{(2\pi\hbar)^2}\int_0^{2\pi} d\Theta\left(\frac{\partial f[\varepsilon_1(P,\Theta)]}{\partial\varepsilon_1(P,\Theta)} + \frac{\partial f[\varepsilon_2(P,\Theta)]}{\partial\varepsilon_2(P,\Theta)}\right)\cos^2\Theta\, u_x. \quad (41)$$

Using the definition of the density for the normal component from Eq. (40), we obtain

$$\rho_n^{(xx)}(T)=\frac{s}{k_BT}\int_0^{\infty}dP\frac{P^3}{(2\pi\hbar)^2}\times\int_0^{2\pi}d\Theta\left(\frac{\exp[\varepsilon_1(P,\Theta)/(k_BT)]}{\{[\exp[\varepsilon_1(P,\Theta)/(k_BT)]-1\}^2}+\frac{\exp[\varepsilon_2(P,\Theta)/(k_BT)]}{\{[\exp[\varepsilon_2(P,\Theta)/(k_BT)]-1\}^2}\right)\cos^2\Theta. \tag{42}$$

Furthermore, from Eq. (39), we can also obtain

$$J_y=-\frac{s}{k_BT}\int_0^{\infty}\frac{d^2P}{(2\pi\hbar)^2}P_xP_y\left(\frac{\partial f[\varepsilon_1(P,\Theta)]}{\partial\varepsilon_1(P,\Theta)}+\frac{\partial f[\varepsilon_2(P,\Theta)]}{\partial\varepsilon_2(P,\Theta)}\right)u_x, \tag{43}$$

which we can expand into the following form

$$J_y=\frac{s}{k_BT}\int_0^{\infty}dP\frac{P^3}{(2\pi\hbar)^2}\times\int_0^{2\pi}d\Theta\left(\frac{\exp[\varepsilon_1(P,\Theta)/(k_BT)]}{\{[\exp[\varepsilon_1(P,\Theta)/(k_BT)]-1\}^2}+\frac{\exp[\varepsilon_2(P,\Theta)/(k_BT)]}{\{[\exp[\varepsilon_2(P,\Theta)/(k_BT)]-1\}^2}\right)\cos\Theta\sin\Theta\;u_x. \tag{44}$$

The integral in Eq. (43) is zero, since the Θ integral over the period of the integrand vanishes. Therefore one determines that $\rho_n^{(xy)}=0$. Now, assuming that the vector $\mathbf{u}$ is parallel to the OY axis, we obtain analogously the following relations:

$$\rho_n^{(yy)}(T)=\frac{s}{k_BT}\int_0^{\infty}dP\frac{P^3}{(2\pi\hbar)^2}\int_0^{2\pi}d\Theta\left(\frac{\exp[\varepsilon_1(P,\Theta)/(k_BT)]}{\{[\exp[\varepsilon_1(P,\Theta)/(k_BT)]-1\}^2}+\frac{\exp[\varepsilon_2(P,\Theta)/(k_BT)]}{\{[\exp[\varepsilon_2(P,\Theta)/(k_BT)]-1\}^2}\right)\sin^2\Theta, \tag{45}$$

$$\rho^{(yx)}(T)=0. \tag{46}$$

By defining the tensor of the concentration of the normal component as the linear response of the flow of quasiparticles on the external velocity as $n_n^{(ij)}=\rho_n^{(ij)}/M_i$, one obtains

$$n_n^{(xx)}(T)=\frac{s}{k_BM_xT}\int_0^{\infty}dP\frac{P^3}{(2\pi\hbar)^2}\times\int_0^{2\pi}d\Theta\left(\frac{\exp[\varepsilon_1(P,\Theta)/(k_BT)]}{\{[\exp[\varepsilon_1(P,\Theta)/(k_BT)]-1\}^2}+\frac{\exp[\varepsilon_2(P,\Theta)/(k_BT)]}{\{[\exp[\varepsilon_2(P,\Theta)/(k_BT)]-1\}^2}\right)\cos^2\Theta, \tag{47}$$

$$n_n^{(yy)}(T)=\frac{s}{k_BM_yT}\int_0^{\infty}dP\frac{P^3}{(2\pi\hbar)^2}\times\int_0^{2\pi}d\Theta\left(\frac{\exp[\varepsilon_1(P,\Theta)/(k_BT)]}{\{[\exp[\varepsilon_1(P,\Theta)/(k_BT)]-1\}^2}+\frac{\exp[\varepsilon_2(P,\Theta)/(k_BT)]}{\{[\exp[\varepsilon_2(P,\Theta)/(k_BT)]-1\}^2}\right)\sin^2\Theta, \tag{48}$$

$$n^{(xy)}(T)=0,\quad n^{(yx)}(T)=0. \tag{49}$$

The linear response of the flow of quasiparticles $\mathbf{J}_{qp}$ with respect to the external velocity at any angle measured from the OX direction is given in terms of the angle-dependent concentration for the normal component $\tilde{n}_n(\Theta,T)$ as

$$|\mathbf{J}_{qp}|=\left|n_n^{(xx)}(T)\,u_x\,\mathbf{i}+n_n^{(yy)}(T)\,u_y\,\mathbf{j}\right|=\sqrt{\left[n_n^{(xx)}(T)\right]^2u^2\cos^2\Theta+\left[n_n^{(yy)}(T)\right]^2u^2\sin^2\Theta}=\tilde{n}(\Theta,T)u, \tag{50}$$

where the concentration of the normal component is

$$\tilde{n}_n(\Theta,T)=\sqrt{\left[n_n^{xx}(T)\right]^2\cos^2\Theta+\left[n_n^{yy}(T)\right]^2\sin^2\Theta}. \tag{51}$$

From Eq. (51), it follows that $n_n^{(xx)}=\tilde{n}_n(\Theta=0)$ and $n_n^{(yy)}=\tilde{n}_n(\Theta=\pi/2)$. We can then rewrite Eq. (51) in the following form:

$$\tilde{n}_n(\Theta,T)=\sqrt{\frac{\left[n_n^{xx}(T)\right]^2+\left[n_n^{yy}(T)\right]^2}{2}+\frac{\left(\left[n_n^{xx}(T)\right]^2-\left[n_n^{yy}(T)\right]^2\right)\cos(2\Theta)}{2}}. \tag{52}$$

We define the angle-dependent concentration of the superfluid component $\tilde{n}_s(\Theta,T)$ by

$$\tilde{n}_s(\Theta,T)=n-\tilde{n}_n(\Theta,T), \tag{53}$$

where n is the total concentration of the excitons. The mean-field critical temperature $T_c(\Theta)$ of the phase transition related to the occurrence of superfluidity in the direction with the angle Θ relative to the x direction is determined by the condition $\tilde{n}_n(\Theta,T)=n$.

In a straightforward way, it follows from Eq. (32) that for $j=2$ the sound velocity vanishes. Therefore we only take into account the spectrum of collective excitations for $j=1$. According to Ref. [31], it is clear that we need a finite sound velocity for superfluidity. Since the branch of collective excitations at zero sound velocity corresponds to zero energy of the quasiparticles (which means that no quasiparticles are created at zero sound velocity), this branch does not lead to dissipation of energy, thereby resulting in finite velocity and does not affect the Landau critical velocity. The weakly interacting gas of dipolar excitons, satisifies the Landau criterion for superfluidity since for small momenta, the energy spectrum of the quasiparticles in the weakly interacting gas of dipolar excitons at $j=1$ is soundlike with sound velocity

$$c_1(\Theta)=\sqrt{\frac{gn_A}{M_{OA}(\Theta)}+\frac{gn_B}{M_{OB}(\Theta)}}. \tag{54}$$

Clearly, the ideal Bose gas does not have a branch with nonzero sound velocity, thereby not demonstrating superfluidity. At low temperatures, the two-component system of dipolar excitons exhibits superfluidity due to exciton-exciton interactions. With this new knowledge, we can again return to our definition for the mass current in Eq. (39) rewritten as

$$\mathbf{J} = s\int \frac{d^2P}{(2\pi\hbar)^2}\mathbf{P} f[\varepsilon_1(P,\Theta) - \mathbf{P}\cdot\mathbf{u}], \tag{55}$$

where $s = 16$ is the spin degeneracy factor, $f[\varepsilon_1(p)]$ is the Bose-Einstein distribution function for the quasiparticles with dispersion $\varepsilon_1(p)$ and k_B is the Boltzmann constant. Expanding this to first order with respect to $\mathbf{P}\cdot\mathbf{u}/(k_BT)$, we obtain

$$\mathbf{J} = -s\frac{\mathbf{u}}{2}\int \frac{d^2P}{(2\pi\hbar)^2}P^2\frac{\partial f[\varepsilon_1(P,\Theta)]}{\partial\varepsilon_1(P,\Theta)}. \tag{56}$$

The density of the normal component ρ_n, in the moving weakly interacting Bose gas of dipolar excitons is defined as $\mathbf{J} = \rho_n\mathbf{u}$. Therefore

$$\rho_n = -\frac{s}{2}\int \frac{d^2P}{(2\pi\hbar)^2}P^2\frac{\partial f[\varepsilon_1(P,\Theta)]}{\partial\varepsilon_1(P,\Theta)}. \tag{57}$$

By substituting the sound velocity $\varepsilon_1(P,\Theta) = c_1(\Theta)P$ into Eq. (57), we obtain

$$\rho_n(T) = \frac{3s\zeta(3)}{2\pi\hbar^2c_1^4(\Theta)}k_B^3T^3. \tag{58}$$

The mean field critical temperature T_c of the phase transition at which the superfluidity occurs, implying neglecting the interaction between the quasiparticles, is obtain from the condition $\rho_s(T_c) = 0$:

$$\rho_n(T_c,\Theta) = \rho = M_{OA}n_A + M_{OB}n_B. \tag{59}$$

At low temperatures $k_BT \ll M_{A(B)}c_1(\Theta)^2$, by substituting Eq. (59) into Eq. (58) one derives

$$T_c(\Theta) = \left[\frac{2\pi\hbar^2\rho c_1^4(\Theta)}{3\zeta(3)sk_B^3}\right]^{1/3}. \tag{60}$$

In this paper, we have obtained the mean-field critical temperature T_c of the phase transition at which superfluidity appears without claiming BEC in a 2D system at finite temperature.

V. RESULTS AND DISCUSSION

A. Computation of sound velocity as functions of chosen parameters

We now demonstrate numerically the dependence of the sound velocity and the critical temperature on the angle Θ and chosen parameters for an experiment such as the interlayer separation D and the relative value of the out-of-plane electric field α. It is worth noting that the formalism outlined above can apply to any mixtures of excitons - A and B, A and C, and B and C exciton mixtures. For the masses in this section, we will be looking at the non-Floquet engineered masses specified via Eq. (9).

In Fig. 7, the sound velocity c_1 is plotted as a function of the angle Θ. The sound velocity is seen to have a maximum at $\pi/2$ and $3\pi/2$ and is minimum at π and 2π. The sound velocity oscillates for all mixtures of excitons and has maxima at around 1.5×10^5 m/s for all mixtures of excitons for the parameters we have chosen below. The minima are about 8.0×10^4 m/s.

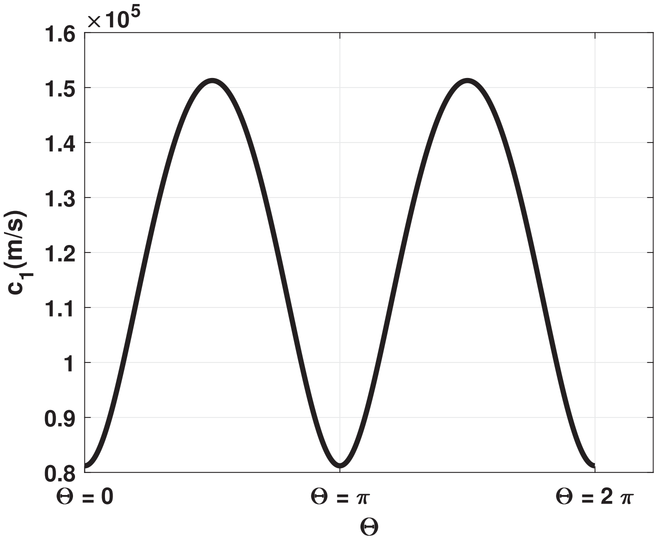

FIG. 7. Plot of the sound velocity c_1 as a function of Θ for the mixing of type A and B excitons. The difference in the sound velocity for different mixtures of excitons, as a function of Θ is negligibly small. The parameters that have been kept constant for this are $n = 1\times10^{11}$ cm^{-2}, $D = 25$ nm, and $\alpha = 35$. We employed the definition of the sound velocity in Eq. (37) in the generation of these figures.

In Fig. 8 below, we plot the dependence of the sound velocity c_1 as a function of the interlayer separation D (nm). It is worth noting that higher values of interlayer separation lead to higher sound velocities for all mixtures of excitons; It is worth noting that at our recommended number h-BN

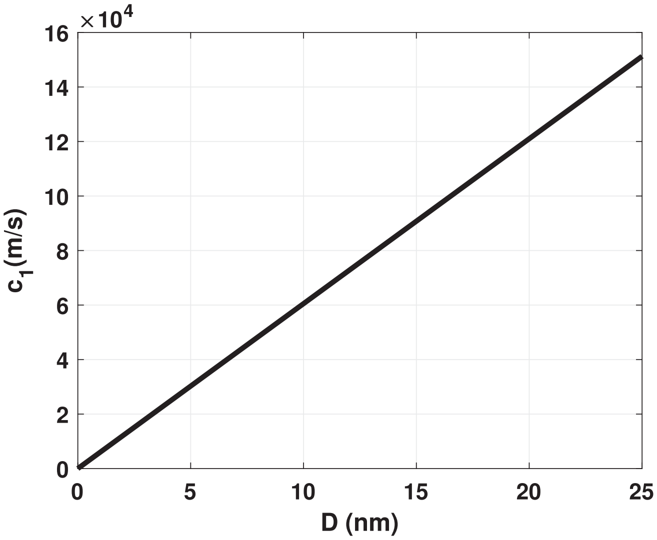

FIG. 8. Plot of the sound velocity c_1 as a function of D for different mixtures of excitons. The difference in the sound velocity for different mixtures of excitons, as a function of D is negligibly small. The parameters that have been kept constant for this are $n = 1\times10^{11}$ cm^{-2}, $\alpha = 35$, and $\Theta = \pi/2$. We employed the definition of the sound velocity in Eq. (37) in the generation of these figures.

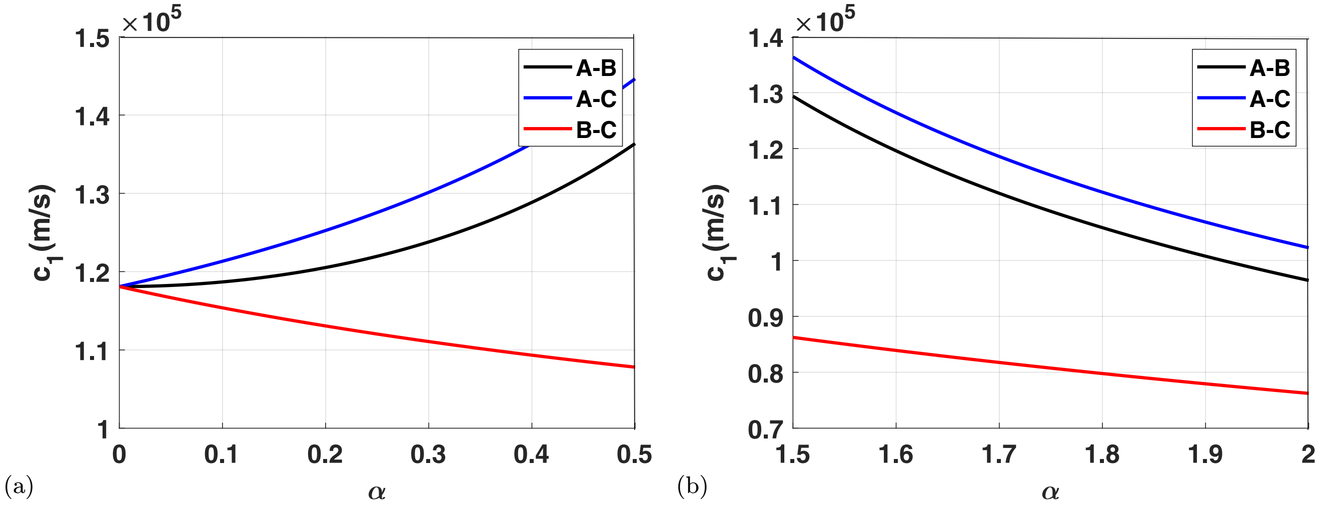

FIG. 9. Plot of the sound velocity c_1 as a function of α for different mixtures of excitons, for the following ranges of α: (a) $0 \leqslant \alpha \leqslant 0.5$ and (b) $1.5 \leqslant \alpha \leqslant 2.0$. The parameters that have been kept constant for this are $n = 1 \times 10^{11}$ cm^{-2}, $D = 3.3$ nm, and $\Theta = \pi/2$. We employed the definition of the sound velocity in Eq. (37) in the generation of these figures.

layers—10 layers at 3.3 Å per layer for an interlayer separation of 3.3 nm—the sound velocity is around 2 x 10^4 m/s.

In Fig. 9, we plot the sound velocity as a function of the relative value α of the out-of-plane electric field. For A-B exciton mixtures, and A-C exciton mixtures, the sound velocity initially has a base value which increases in the range $0 < \alpha < 0.5$. A-C exciton mixtures have higher sound velocity at low values of α. When $\alpha = 1.0$, there is no calculated sound velocity because at this critical value of α, the A excitons have zero total mass, as demonstrated in Fig. 2(b). The sound velocity is monotonically decreasing beyond $\alpha > 1.5$. A-C exciton mixtures have consistently higher sound velocities compared to A-B exciton mixtures but only negligibly. For B-C exciton mixtures, the sound velocity decreases for increasing values of α.

B. The critical temperature

We now turn our attention to calculating the critical temperature as functions of various chosen parameters. We begin by investigating the dependence of the critical temperature as a function of the angle Θ shown in Fig. 10. As expected, the behavior here is also oscillatory, displaying similar maxima and minima as the dependence of the sound velocity on the angle Θ. The different mixtures of excitons demonstrate negligibly different critical temperatures. When zoomed in the A and C exciton mixtures display generally higher critical temperatures, and B and C exciton mixtures display generally lower critical temperatures, but notably the difference is a very small percentage of their mean value.

We plot the critical temperature as a function of the interlayer separation D, in Fig. 11. We chose the range 3.0 nm $\leqslant D \leqslant$ 6.0 nm since this is a range of interest for a feasible number of h-BN layers in an experiment. This smaller range also helps us see with greater resolution the contrast between the different mixtures of excitons. Larger interlayer separations lead to higher critical temperatures.

We now investigate the critical temperature for superfluidity as a function of α. Our results are presented in Fig. 12. The critical temperature is increased in the range $0 < \alpha < 0.5$ for A-B and A-C exciton mixtures. At $\alpha = 1.0$, the critical temperature is notably unable to be calculated because of the zero total mass of A excitons. For all mixtures of excitons, the critical temperature for superfluidity is decreased beyond $\alpha > 1.5$. Zooming in, one can see that the A-C exciton mixtures have a higher critical temperature than the other two exciton mixtures at low values of α, while A-B exciton mixtures have a higher critical temperature than A-C exciton mixtures, past $\alpha = 0.4$, but only negligibly. The B-C exciton mixtures have the lowest critical temperature for superfluidity, compared to other exciton mixtures, for any chosen set of parameters.

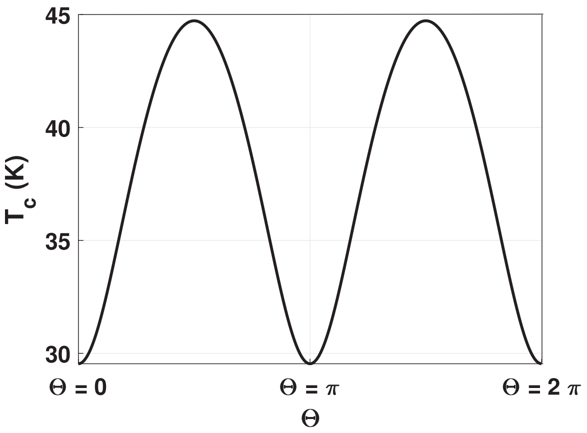

FIG. 10. The dependence of the critical temperature as a function of Θ for different mixtures of A and B excitons. The difference in the critical temperature for different mixtures of excitons, as a function of Θ is negligibly small. The parameters that have been kept constant for this are $n = 20 \times 10^{11}$ cm^{-2}, $D = 3.3$ nm, and $\alpha = 35$. We employed the definition of the critical temperature, T_c in Eq. (60) in the generation of these figures.

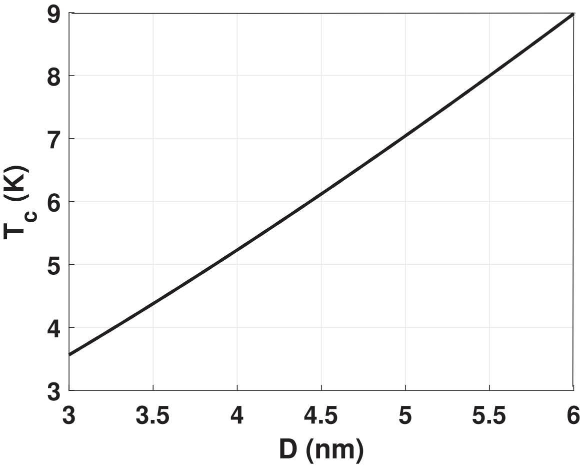

FIG. 11. The dependence of the critical temperature as a function of D for different mixtures of excitons. The difference in the critical temperature for different mixtures of excitons, as a function of D is negligibly small. The parameters that have been kept constant for this are $n = 1 \times 10^{11}\mathrm{cm}^{-2}$, $\Theta = \pi/2$, and $\alpha = 35$. We employed the definition of the critical temperature, T_c in Eq. (60) in the generation of these figures.

Since using a large values of α is favorable for a larger exciton binding energy, and thus stability and lifetime of the exciton, we need to balance the choice of the parameter with the diminishing of the critical temperature T_c for superfluidity.

It is worth calculating the critical temperature for the set of experimental parameters we recommend. These are as a function of the exciton concentration n, where $n = n_A/2 = n_B/2$. For this calculation, we set the parameters as follows: $\alpha = 35.0$, $D = 3.3$ nm, (corresponding to ten layers of h-BN) and $\Theta = \pi/2$. Our results are presented in Fig. 13. All mixtures of excitons lead to fairly similar critical temperatures for different concentrations of excitons. Since we consider the dilute limit, we demand that the average distance between the excitons is much larger than the interlayer separation. Mathematically, this corresponds to $n \ll 1/(\pi D^2)$.

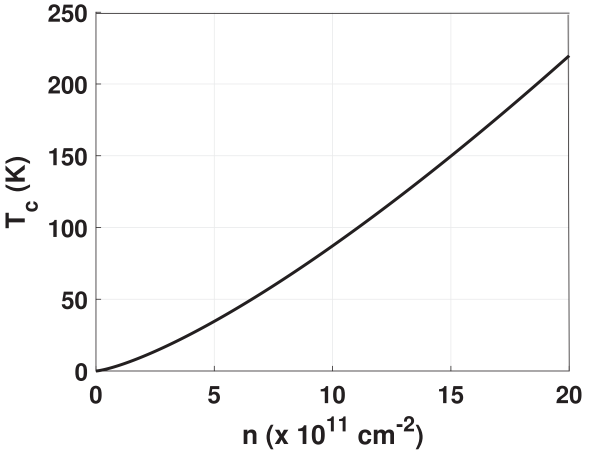

FIG. 13. Plot of the critical temperature as a function of n for different mixtures of excitons. The difference in the critical temperature for different mixtures of excitons, as a function of n is negligibly small. The parameters that have been kept constant for this are $\alpha = 35$, $\Theta = \pi/2$, and $D = 3.3$ nm. We employed the definition of the critical temperature, T_c in Eq. (60) in the generation of these figures.

It is not necessary to restrict our attention to the condition $n = n_A/2 = n_B/2$, for any two mixtures of excitons. As such, in Fig. 14, we investigate the dependence of T_c as a function of the exciton densities. We notice that an increase in exciton density for both types of excitons leads to a higher critical temperature. We note that the increase in concentration to a value of $n_A = n_B = 2.0 \times 10^{12}$ cm^{-2}, leads to a critical temperature of around $T_c = 250$ K, which holds true for any combination of any two excitons of A, B, or C. It is worth noting that in the mixing of B and C excitons, the concentration of B excitons has a more pronounced effect on the T_c.

VI. CONCLUSIONS AND DISCUSSION

In this paper, we have investigated the binding energies, wave functions, collective properties and superfluidity of

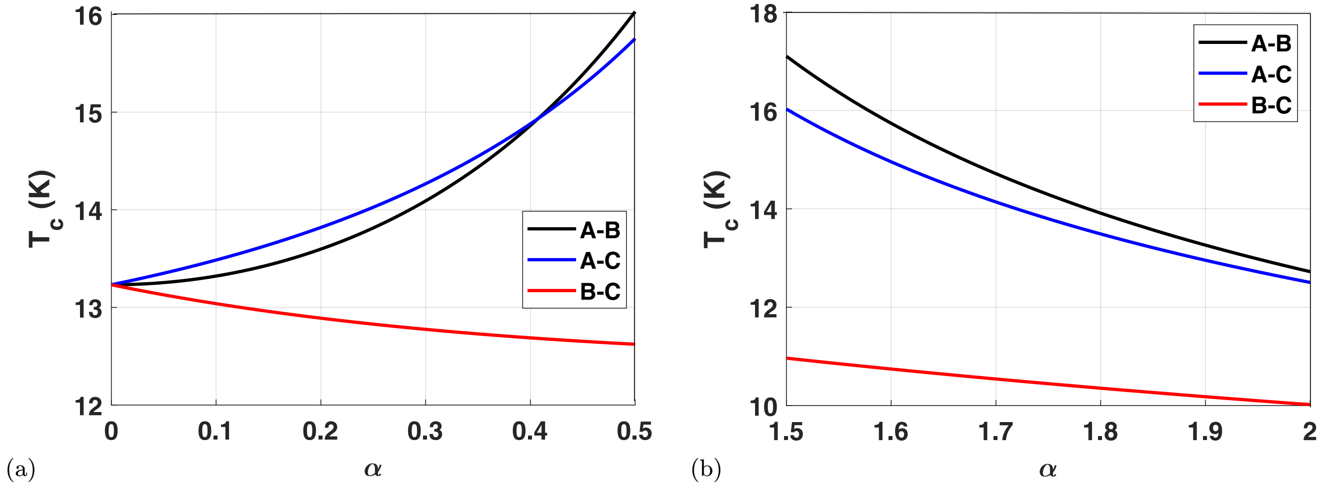

FIG. 12. Plot of the critical temperature as a function of α for different mixtures of excitons, for the following ranges of α: (a) $0 \leqslant \alpha \leqslant 0.5$ and (b) $1.5 \leqslant \alpha \leqslant 2.0$. The parameters that have been kept constant for this are $n = 1 \times 10^{11}$ cm^{-2}, $\Theta = \pi/2$, and $D = 3.3$ nm. We employed the definition of the critical temperature, T_c in Eq. (60) in the generation of these figures.

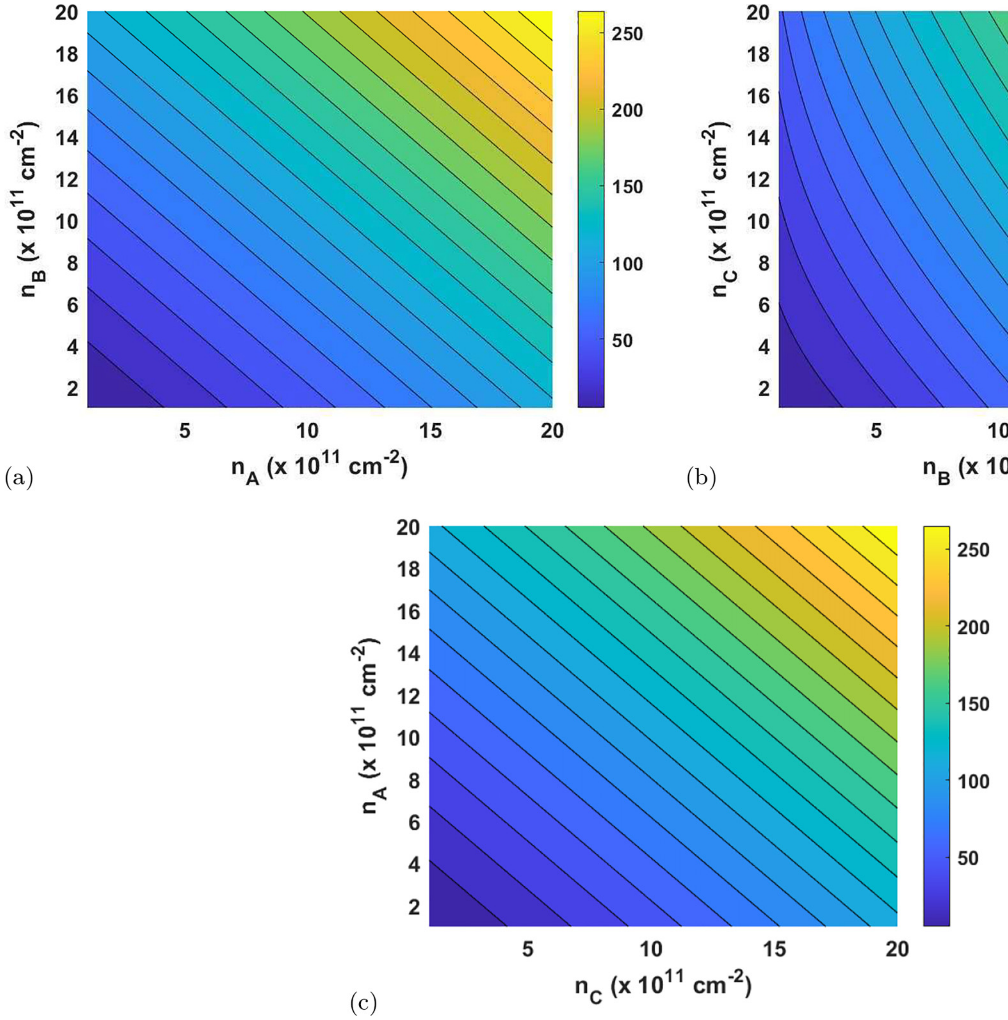
(a)
(b)
(c)

FIG. 14. Plot of the critical temperature as a function of the exicton densities for different mixtures of excitons. The parameters that have been kept constant for this are $\alpha = 35$, $\Theta = \pi/2$, and $D = 3.3$ nm. The colorbar on the side is the critical temperature T_c in Kelvins. We employed the definition of the critical temperature, T_c in Eq. (60) in the generation of these figures.

dipolar excitons in a double layer of massive anisotropic tilted Dirac systems irradiated by circularly polarized light. For our calculations as an example we have considered a double layer of 1T′-MoS$_2$. The binding energy of the three different types of excitons has been obtained by employing the harmonic oscillator approximation. It is found that using a large value of a perpendicular electric field α leads to a large binding energy at a small enough interlayer separation D to use an experimentally reasonable number of layers of h-BN dielectric. It is also found that using Floquet engineering of the energy bands leads to no appreciable change in the effective mass of the electrons or holes. However, it is worth noting that it is unclear if using a larger λ_0 value, corresponding to a larger irradiation intensity to frequency ratio would lead to an appreciable increase in the effective mass. To study this, a second-order or higher expansion of the energy dispersion would be necessitated. However, as seen in Fig. 6, the binding energy of the excitons is very close in magnitude to the binding energy without any circularly polarized dressing field applied.

We note that for dipolar excitons in 1T′-MoS$_2$, the spectrum of collective excitations is angular dependent. Furthermore, for dipolar excitons in double-layer 1T′-MoS$_2$, the normal and superfluid concentrations have a tensor form whose components depend on the direction of exciton flow. Additionally, for the double-layer, the mean-field critical temperature of superfluidity depends on the direction of exciton flow as demonstrated in Fig. 10. Therefore the influence of the anisotropy of the dispersion relation of dipolar excitons in a double layer of 1T′-MoS$_2$ with tilted Dirac bands has been investigated. We conclude that the anisotropy of the energy band structure of the in 1T′-MoS$_2$ exhibits tunable superfluidity at low to high temperatures. The presence of an exciton superfluid has direct applications in dissipationless solid-state excitonics [43]. The search for high-temperature superfluidity has also yielded significant theoretical work in investigating whether the doping of coupled monolayers switches the system from one component to two component dependent superfluidity [44], and approaches to creating three-dimensional superfluidity involving creating a superlattice of doped monolayers of TMDCs to avoid strong two-dimensional fluctuations and Kosterlitz-Thouless effects [44]. It is crucial to note that the binding energy of dipolar excitons and mean-field critical temperature for superfluidity are sensitive to the electron and hole effective masses. In terms of experimental observation, we can exploit some features of the photoluminescence spectrum, including emission traces caused by phonon-assisted recombination of momentum-space dark excitons. The microscopic theory for this was recently developed [45]. The theory can be applied specifically to the case of momentum-space dark excitons in a double layer of 1T′-MoS$_2$. This warrants further development of the formalism in conjunction with analysis of experimental results of phonon-assisted photoluminiscence experiments. Experimental findings include the observation of intervalley momentum-forbidden excitons influenced by compressive strain, serving as an ultrasensitive optical strain sensing mechanism, and the repulsion-driven propagation of dark spin-forbidden excitons, allowing for the propagation of valley and spin information across TMD samples for diverse optoelectronic applications [5–7]. It is also worth noting that recent studies have demonstrated that a Dirac exciton, possesses an intrinsic angular momentum, which modifies the exciton spectrum and introduces corrections that are worth future study in particular [46,47]. These properties may be investigated especially in conjuction with methods of synthesis that modify TMDC properties [48]. We hope that our analytical and numerical results will provide motivation for future experimental and theoretical investigations regarding the effects of circularly polarized light on excitonic BEC and superfluidity for double layer 1T′-MoS$_2$.

ACKNOWLEDGMENTS

The authors are grateful to O. V. Roslyak and A. Shklyarevsky for valuable discussions. G.G. acknowledges the support from the US Air Force Research Laboratory (AFRL) Grant No. FA9453-21-1-0046.

APPENDIX: FLOQUET ENGINEERING OF TILTED AND GAPPED DIRAC BAND STRUCTURE

1. Circularly polarized dressing field

It has been suggested that applying an external high-frequency optical dressing field of variable intensity, within the off-resonance regime, can modify the band structure, anisotropy, and band gaps of 1T′-MoS$_2$ [49]. Additionally, it was demonstrated that the electron-photon dressed states vary strongly with the polarization of the applied irradiation and reflect a full complexity of the low-energy Hamiltonian for nonirradiated material. Employing the numerical results for the dressed states obtained by using circularly polarized irradiation, derived in Ref. [49], we calculate the effective masses of the electron and hole using the following dispersion of irradiated subbands given by Eq. (A1), with the hope of leveraging the frequency and intensity variables that allow for higher binding energies, and parameterise the superfluidity [49]. We have

$$\varepsilon_{\tau=\pm1}(\mathbf{k}|\xi,s) = -\hbar\xi\upsilon_{-}k_y \pm \hbar\sqrt{\tilde{\Delta}^2_{\xi|s}(\lambda_0) + [(\xi - s\alpha)\Delta_0 + \upsilon_2 k_y]^2 + (\upsilon_{+}k_y)^2 + (\upsilon_1 k_x)^2}, \tag{A1}$$

where the additional irradiation-induced band gap $\tilde{\Delta}_{\xi|s}(\lambda_0)$ takes the explicit form

$$\tilde{\Delta}_{\xi|s}(\lambda_0) = \pm\sqrt{2c_0^2\upsilon_1\upsilon_{+}\Delta_0(1 - s\alpha\xi) + c_0^4\upsilon_1^2\left(\upsilon_2^2 + \upsilon_{+}^2\right)}, \tag{A2}$$

and $\lambda_0 = v_F eE_0/(\hbar\omega^2) \ll 1$, υ_-, υ_+, υ_1 and υ_2 are as defined above as the Fermi velocities and the velocity correction terms. Furthermore, $\tau = \pm1$ labels the electron/hole states related to the conduction and the valence bands, while $s = \pm1$ is the real spin index. The spin-orbit coupling gap is $\Delta_0 = 0.81E^{(0)}$, $\alpha = |E_z/E_c|$ is the relative value for the out-of-plane electric field, and E_c stands for a critical field at which the band gap in 1T′-MoS$_2$ will be closed. It is important to notice that the energy dispersions are spin and valley polarized, i.e., depend directly on indices s and ξ. It is worth noting that the dressed states formed using linearly polarized dressing field are not studied in this paper.

The model Hamiltonian within the effective mass approximation for a single electron-hole pair in a 1T′-MoS$_2$ double layer is given by

$$\hat{H}_0 = -\frac{\hbar^2}{2m_x^e}\frac{\partial^2}{\partial x_1^2} - \frac{\hbar^2}{2m_y^e}\left[\frac{\partial}{\partial y_1} - p_e^{(0)}\right]^2 - \frac{\hbar^2}{2m_x^h}\frac{\partial^2}{\partial x_2^2} - \frac{\hbar^2}{2m_y^h}\left[\frac{\partial}{\partial y_2} - p_h^{(0)}\right]^2 + V(\sqrt{r^2 + D^2}), \tag{A3}$$

where $V(\sqrt{r^2 + D^2})$ is the potential energy for electron-hole pair attraction, when the electron and hole are located in two different 2D planes. In Eq. (A3), m_x^e, m_y^e, m_x^h, m_y^h, $p_e^{(0)}$, and $p_h^{(0)}$ are the constants, which can be obtained from Eq. (A4) using the method of completing the square as seen below. Using the long wavelength expansion we obtain

$$\begin{aligned}\varepsilon_{\tau=\pm1}(\mathbf{k}|\xi,s) = {}& \hbar\left(\frac{\Delta_0\upsilon_2(\xi - \alpha s)}{\sqrt{\Delta_0^2(\xi - \alpha s)^2 + \tilde{\Delta}^2_{\xi|s}(\lambda_0)}} - \xi\upsilon_{-}\right)k_y \\ & \pm\left(\sqrt{\Delta_0^2(\xi - \alpha s)^2 + \tilde{\Delta}^2_{\xi|s}(\lambda_0)} + \frac{\hbar^2\upsilon_1^2}{2\sqrt{\Delta_0^2(\xi - \alpha s)^2 + \tilde{\Delta}^2_{\xi|s}(\lambda_0)}}k_x^2\right. \\ & \left. + \frac{\hbar^2\left(\Delta_0^2\upsilon_{+}^2(\xi - \alpha s)^2 + \tilde{\Delta}^2_{\xi|s}(\lambda_0)\left(\upsilon_2^2 + \upsilon_{+}^2\right)\right)}{2\left[\Delta_0^2(\xi - \alpha s)^2 + \tilde{\Delta}^2_{\xi|s}(\lambda_0)\right]^{3/2}}k_y^2\right).\end{aligned} \tag{A4}$$

From Eq. (A4), we are able to deduce the following quantities

$$m_x^{e/h} = \frac{\sqrt{\Delta_0^2(\xi - \alpha s)^2 + \tilde{\Delta}_{\xi|s}^2(\lambda_0)}}{\upsilon_1^2}, \quad m_y^{e/h} = \frac{\left[\Delta_0^2(\xi - \alpha s)^2 + \tilde{\Delta}_{\xi|s}^2(\lambda_0)\right]^{3/2}}{\Delta_0^2\upsilon_+^2(\xi - \alpha s)^2 + \tilde{\Delta}_{\xi|s}^2(\lambda_0)\left(\upsilon_2^2 + \upsilon_+^2\right)}, \tag{A5}$$

$$\tilde{p}_{e/h}^{(0)} = \mp\frac{\left(\Delta_0^2(\xi - \alpha s)^2 + \tilde{\Delta}_{\xi|s}^2(\lambda_0)\right)(\alpha s \upsilon_2 \Delta_0 - \upsilon \Delta_0 \xi + \upsilon_- \xi)}{\upsilon_+^2\Delta_0^2(\xi - \alpha s)^2 + \left(\upsilon_2^2 + \upsilon_+^2\right)\tilde{\Delta}_{\xi|s}^2(\lambda_0)}, \tag{A6}$$

where $m_x^{e/h}$ and $m_y^{e/h}$ denote the effective masses of the electron and hole in the x and y directions respectively and $\tilde{p}_{e/h}^{(0)}$ is an effective constant that reflect the anisotropy of the system. The solutions to the equation of motion for the center-of-mass and relative motion of the electron-hole pair are identical to those described in Sec. I B, with the constants being the only difference.

2. Binding energy

In this section, we compute the binding energies of the excitons for chosen parameters. For our calculations, we confine our attention to $\xi = 1.0$. We perform calculations for both combinations of spins, spin up ($s_e = +1$) electrons and spin down holes, and spin down electrons ($s_e = -1$) and spin up holes. In our calculations, it is worth noting that the mass of the holes is effectively that of an electron of opposite spin. In Fig. 15, the irradiation intensity $\mathcal{I}_{df} = 10^9$, the frequency of irradiation $\omega = 10^{16}$ Hz, and the relative value of the out-of-plane electric field $\alpha = 35.0$. Our calculations show that spin down electrons-spin up hole pairs have a higher binding energy than spin up electrons-spin down hole pairs. These binding energies are also on a similar scale as the results outlined in Sec. I D in particular Figs. 3(b), 4(b) and 5(b).

It is worth considering certain parameter restrictions and suggestions. This would enable us to obtain the binding energies for chosen interlayer eparation. Our choice of parameters leads to a higher binding energy for smaller interlayer separation. We find that choosing a α of larger magnitude, leads to this effect. Additionally, the value of the gap must be real and positive.

Additionally, it is worth noting that changing ω and $\mathcal{I}_{df}$ does not induce an appreciable change in the effective masses.

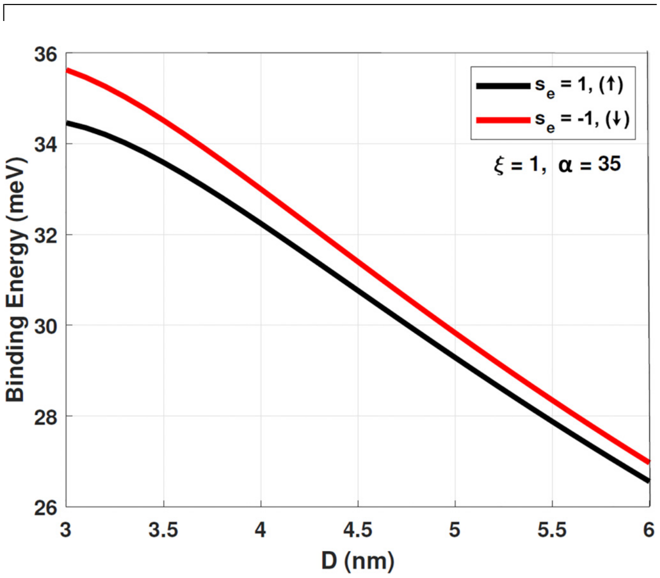

FIG. 15. Relationship between the binding energies of excitons and interlayer separation D for spin up (black) and spin down (red) electron-hole pairs. These results are for intravalley excitons at $\xi = 1$. The following combination of parameters is used for each of the binding energy calculations: $\mathcal{I}_{df} = 10^9$, $\omega = 10^{16}$ Hz, and $\alpha = 35$. We employed the binding energy definition of Eq. (29), along with the effective mass definitions of Eq. (A5), in the generation of these figures.

In accordance with prior results [49], we find that the larger band gaps tend to be reduced by circularly polarized dressing field. The orientation and anisotropy for the constant-energy cut dispersions in 1T′-MoS$_2$ remains unchanged under circularly polarized irradiation. The additional energy gap induced by the irradiation is contributed by the $\tilde{\Delta}$ term in Eq. (A2).

[1] K. F. Mak, D. Xiao, and J. Shan, Light-valley interactions in 2D semiconductors, Nature Photon **12**, 451 (2018).

[2] S. Joseph, J. Mohan, S. Lakshmy, S. Thomas, B. Chakraborty, S. Thomas, and N. Kalarikkal, A review of the synthesis, properties, and applications of 2D transition metal dichalcogenides and their heterostructures, Mater. Chem. Phys. **297**, 127332 (2023).

[3] T. LaMountain, J. Nelson, E. J. Lenferink, S. H. Amsterdam, A. A. Murthy, H. Zeng, T. J. Marks, V. P. Dravid, M. C. Hersam, and N. P. Stern, Valley-selective optical stark effect of exciton-polaritons in a monolayer semiconductor, Nat. Commun. **12**, 4530 (2021).

[4] A. Sinner, Y. E. Lozovik, and K. Ziegler, Pairing transition in a double layer with interlayer coulomb repulsion, Phys. Rev. Res. **2**, 033085 (2020).

[5] G. Grosso, S. B. Chand, J. M. Woods, and E. Mejia, Controlling dark excitons in two-dimensional TMDs for optoelectronic applications, in *2D Photonic Materials and Devices VI*, edited by A. Majumdar, C. M. Torres Jr., and H. Deng, Vol. PC12423 (SPIE, San Francisco, CA, 2023).

[6] S. B. Chand, J. M. Woods, J. Quan, E. Mejia, T. Taniguchi, K. Watanabe, A. Alú, and G. Grosso, Interaction-driven transport of dark excitons in 2D semiconductors with phonon-mediated optical readout, Nat. Commun. **14**, 3712 (2023).

[7] S. B. Chand, J. M. Woods, E. Mejia, T. Taniguchi, K. Watanabe, and G. Grosso, Visualization of dark excitons in semiconductor monolayers for high-sensitivity strain sensing, Nano Lett. **22**, 3087 (2022).

[8] Y. M. P. Gomes and R. O. Ramos, Superconducting phase transition in planar fermionic models with Dirac cone tilting, Phys. Rev. B **107**, 125120 (2023).

[9] A. Balassis, G. Gumbs, and O. Roslyak, Polarizability, plasmons, and screening in 1T′-MoS$_2$ with tilted Dirac bands, Phys. Lett. A **449**, 128353 (2022).

[10] C.-Y. Tan, C.-X. Yan, Y.-H. Zhao, H. Guo, and H.-R. Chang, Anisotropic longitudinal optical conductivities of tilted Dirac bands in 1T′-MoS$_2$, Phys. Rev. B **103**, 125425 (2021).

[11] K. F. Mak and J. Shan, Photonics and optoelectronics of 2D semiconductor transition metal dichalcogenides, Nature Photon **10**, 216 (2016).

[12] D. Xiao, G.-B. Liu, W. Feng, X. Xu, and W. Yao, Coupled spin and valley physics in monolayers of MoS$_2$ and other group-VI dichalcogenides, Phys. Rev. Lett. **108**, 196802 (2012).

[13] T. Cao, G. Wang, W. Han, H. Ye, C. Zhu, J. Shi, Q. Niu, P. Tan, E. Wang, B. Liu, and J. Feng, Valley-selective circular dichroism of monolayer molybdenum disulphide, Nat. Commun. **3**, 887 (2012).

[14] B. Chen, D. Chao, E. Liu, M. Jaroniec, N. Zhao, and S.-Z. Qiao, Transition metal dichalcogenides for alkali metal ion batteries: Engineering strategies at the atomic level, Energy Environ. Sci. **13**, 1096 (2020).

[15] M. Bernardi, M. Palummo, and J. C. Grossman, Extraordinary sunlight absorption and one nanometer thick photovoltaics using two-dimensional monolayer materials, Nano Lett. **13**, 3664 (2013).

[16] A. J. Leggett, Bose-Einstein condensation in the alkali gases: Some fundamental concepts, Rev. Mod. Phys. **73**, 307 (2001).

[17] Z. Wang, D. A. Rhodes, K. Watanabe, T. Taniguchi, J. C. Hone, J. Shan, and K. F. Mak, Evidence of high-temperature exciton condensation in two-dimensional atomic double layers, Nature (London) **574**, 76 (2019).

[18] M. Van der Donck, S. Conti, A. Perali, A. R. Hamilton, B. Partoens, F. M. Peeters, and D. Neilson, Three-dimensional electron-hole superfluidity in a superlattice close to room temperature, Phys. Rev. B **102**, 060503(R) (2020).

[19] Yu. E. Lozovik and V. I. Yudson, On the ground state of the two-dimensional non-ideal Bose gas, Physica A **93**, 493 (1978).

[20] M. M. Fogler, L. V. Butov, and K. S. Novoselov, High-temperature superfluidity with indirect excitons in van der Waals heterostructures, Nat. Commun. **5**, 4555 (2014).

[21] O. L. Berman and R. Ya. Kezerashvili, High-temperature superfluidity of the two-component Bose gas in a transition metal dichalcogenide bilayer, Phys. Rev. B **93**, 245410(2016).

[22] O. L. Berman and R. Ya. Kezerashvili, Superfluidity of dipolar excitons in a transition metal dichalcogenide double layer, Phys. Rev. B **96**, 094502 (2017).

[23] Y. Tang, K. F. Mak, and J. Shan, Long valley lifetime of dark excitons in single-layer WSe$_2$, Nat. Commun. **10**, 4047 (2019).

[24] S. Conti, S. Saberi-Pouya, A. Perali, M. Virgilio, F. M. Peeters, A. R. Hamilton, G. Scappucci, and D. Neilson, Electron-hole superfluidity in strained Si/Ge type II heterojunctions, npj Quantum Mater. **6**, 41 (2021).

[25] J. Wang, Y. Che, L. Zhang, and Q. Chen, Enhancement effect of mass imbalance on Fulde-Ferrell-Larkin-Ovchinnikov type of pairing in Fermi-Fermi mixtures of ultracold quantum gases, Sci. Rep. **7**, 39783 (2017).

[26] M. M. Forbes, E. Gubankova, W. V. Liu, and F. Wilczek, Stability criteria for breached-pair superfluidity, Phys. Rev. Lett. **94**, 017001 (2005).

[27] P. Cudazzo, I. V. Tokatly, and A. Rubio, Dielectric screening in two-dimensional insulators: Implications for excitonic and impurity states in graphane, Phys. Rev. B **84**, 085406 (2011).

[28] See Supplemental Material at http://link.aps.org/supplemental/10.1103/PhysRevB.109.224506 for electron-hole interaction in a 1T′-MoS$_2$ double layer, and collective excitation calculations, which contains Ref. [29].

[29] O. L. Berman, R. Ya. Kezerashvili, G. V. Kolmakov, Yu. E. Lozovik, Turbulence in a Bose-Einstein condensate of dipolar excitons in coupled quantum wells, Phys. Rev. B **86**, 045108 (2012).

[30] M. A. Mojarro, R. Carrillo-Bastos, and J. A. Maytorena, Optical properties of massive anisotropic tilted Dirac systems, Phys. Rev. B **103**, 165415 (2021).

[31] L. D. Landau and E. M. Lifshitz, *Quantum Mechanics: Non Relativistic Theory* (Addison-Wesley, Reading, MA, 1958).

[32] E. Prada, J. V. Alvarez, K. L. Narasimha-Acharya, F. J. Bailen, and J. J. Palacios, Effective-mass theory for the anisotropic exciton in two-dimensional crystals: Application to phosphorene, Phys. Rev. B **91**, 245421 (2015).

[33] A. S. Rodin, A. Carvalho, and A. H. Castro Neto, Excitons in anisotropic two-dimensional semiconducting crystals, Phys. Rev. B **90**, 075429 (2014).

[34] F. Jin, R. Roldán, M. I. Katsnelson, and S. Yuan, Screening and plasmons in pure and disordered single- and bilayer black phosphorus, Phys. Rev. B **92**, 115440 (2015).

[35] J. Park, S. Bong, J. Park, E. Lee, and S.-Y. Ju, Hierarchical van Der waals heterostructure strategy to form stable transition metal dichalcogenide dispersions, ACS Appl. Mater. Interfaces **14**, 50308 (2022).

[36] T. C. Berkelbach, M. S. Hybertsen, and D. R. Reichman, Theory of neutral and charged excitons in monolayer transition metal dichalcogenides, Phys. Rev. B **88**, 045318 (2013).

[37] B. Sun and M. S. Pindzola, Bogoliubov modes and the static structure factor for a two-species Bose-Einstein condensate, J. Phys. B: At. Mol. Opt. Phys. **43**, 055301 (2010).

[38] A. A. Abrikosov, L. P. Gorkov, and I. E. Dzyaloshinskii, *Methods of Quantum Field Theory in Statistical Physics* (Prentice-Hall, Englewood Cliffs, NJ 1963).

[39] E. M. Lifshitz and L. P. Pitaevskii, *Statistical Physics, Part 2*, (Pergamon Press, Oxford, 1980).

[40] P. Tommasini, E. J. V. De Passos, A. F. R. De Toledo Piza, M. S. Hussein, and E. Timmermans, Bogoliubov theory for mutually coherent condensates, Phys. Rev. A **67**, 023606 (2003).

[41] O. L. Berman, G. Gumbs, G. P. Martins, and P. Fekete, Superfluidity of dipolar excitons in a double layer of α-T$_3$ with a mass term, Nanomaterials **12**, 1437 (2022).

[42] O. L. Berman, G. Gumbs, and R. Ya. Kezerashvili, Bose-Einstein condensation and superfluidity of dipolar excitons in a phosphorene double layer, Phys. Rev. B **96**, 014505 (2017).

[43] J.-J. Su and A. H. MacDonald, How to make a bilayer exciton condensate flow, Nat. Phys. **4**, 799 (2008).

[44] S. Conti, M. Van Der Donck, A. Perali, F. M. Peeters, and D. Neilson, Doping-dependent switch from one- to two-component superfluidity in coupled electron-hole van der Waals heterostructures, Phys. Rev. B **101**, 220504(R) (2020).

[45] S. Brem, A. Ekman, D. Christiansen, F. Katsch, M. Selig, C. Robert, X. Marie, B. Urbaszek, A. Knorr, and E. Malic, Phonon-assisted photoluminescence from indirect excitons in monolayers of transition-metal dichalcogenides, Nano Lett. **20**, 2849 (2020).

[46] M. Trushin, M. O. Goerbig, and W. Belzig, Model prediction of self-rotating excitons in two-dimensional transition-metal dichalcogenides, Phys. Rev. Lett. **120**, 187401 (2018).

[47] M. Trushin, M. O. Goerbig, and W. Belzig, Exciton spectrum in two-dimensional transition metal dichalcogenides: The role of Diracness, J. Phys.: Conf. Ser. **864**, 012033 (2017).

[48] S. A. Han, R. Bhatia, and S.-W. Kim, Synthesis, properties and potential applications of two-dimensional transition metal dichalcogenides, Nano Convergence **2**, 17 (2015).

[49] A. Iurov, L. Zhemchuzhna, G. Gumbs, D. Huang, W.-K. Tse, K. Blaise, and C. Ejiogu, Floquet engineering of tilted and gapped Dirac bandstructure in 1T′-MoS$_2$, Sci. Rep. **12**, 21348 (2022).